Spring 2014

Hardware implementation of multiple-input multiple-output transceiver for wireless communication

Bing Han

Department: Electrical and Computer Engineering

HARDWARE IMPLEMENTATION OF MULTIPLE-INPUT MULTIPLE-OUTPUT TRANSCEIVER FOR WIRELESS COMMUNICATION

by

Bing Han

A DISSERTATION

Presented to the Faculty of the Graduate School of the

MISSOURI UNIVERSITY OF SCIENCE AND TECHNOLOGY

In Partial Fulfillment of the Requirements for the Degree

DOCTOR OF PHILOSOPHY

in

ELECTRICAL ENGINEERING

2014

Approved by

Yahong Rosa Zheng, Advisor
Chengshan Xiao
Steve Grant
Yiyu Shi
Sriram Chellappan

PUBLICATION DISSERTATION OPTION

This dissertation consists of the following three published or to be published papers, formatted in the style used by the Missouri University of Science and Technology, listed as follows:

Paper I, B. Han, Z. Yang, and Y. R. Zheng, "Efficient Implementation of an Iterative MIMO-OFDM Receiver Using MMSE Interference Cancelation", has been accepted by IET Commun., Feb. 2014. (pages 6–37)

Paper II, B. Han, Z. Yang, and Y. R. Zheng, "FPGA Implementation of QR Decomposition for MIMO-OFDM Using Four CORDIC Cores", has been published in Proc. IEEE ICC, Budapest, Hungary, Jun. 2013. (pages 38–54)

Paper III, B. Han, Y. R. Zheng,"Higher-Rank Principle Kronecker Model for Triply Selective Fading Channels with Experimental Validation", has been accepted by IEEE Trans. Veh. Technol., Apr. 2014. (pages 55–91)

ABSTRACT

This dissertation proposes an efficient hardware implementation scheme for iterative multi-input multi-output orthogonal frequency-division multiplexing (MIMO-OFDM) transceiver. The transmitter incorporates linear precoder designed with instantaneous channel state information (CSI). The receiver implements MMSE-IC (minimum mean square error interference cancelation) detector, channel estimator, low-density parity-check (LDPC) decoder and other supporting modules. The proposed implementation uses QR decomposition (QRD) of complex-valued matrices with four co-ordinate rotation digital computer (CORDIC) cores and back substitution to achieve the best tradeoff between resource and throughput. The MIMO system is used in field test and the results indicate that the instantaneous CSI varies very fast in practices and the performance of linear precoder designed with instantaneous CSI is limited. Instead, statistic CSI had to be used

This dissertation also proposes a higher-rank principle Kronecker model (PKM). That exploits the statistic CSI to simulate the fading channels. The PKM is constructed by decomposing the channel correlation matrices with the higher-order singular value decomposition (HOSVD) method. The proposed PKM-HOSVD model is validated by extensive field experiments conducted for 4-by-4 MIMO systems in both indoor and outdoor environments. The results confirm that the statistic CSI varies slowly and the PKM-HOSVD will be helpful in the design of linear precoders.

ACKNOWLEDGMENTS

I would like to express the deepest appreciation to my advisor, Dr. Yahong Rosa Zheng. Her enthusiasm and dedication towards research have always been a great source of inspiration. Throughout my graduate study, she instructed me in research attitude, specific knowledge, and technical writing. Her advices on both research and career have been priceless. This dissertation would not have been possible without her support and guidance.

My sincere appreciation also goes to Dr. Chengshan Xiao. I greatly appreciate his support and guidance for my course and research work. He provided a lot of technical assistance and good ideas. He also shared his experiences in both research and career which will help me all my life.

I would like to thank the other members of my advisory committee, Drs. Yiyu Shi, Steve Grant and Sriram Chellappan for generously offering their time and invaluable advice for my research.

I would like to thank Dr. Weiliang Zeng. He provided a lot of ideas in my research and technical writing. In addition, I would like to thank Zengli Yang. I enjoyed our collaborations and publications. I would also like to thank Drs. Peng Han and Xinhu Li for their help on the outdoor experiments. I would like to thank all the current and past members in the research lab, including Mingxi Wang, Huang Lou, Yongpeng Wu, Jun Tao, Longbao Wang, Ming Yue, Weimin Duan, Dongjie Bi, Niaz Ahmed and Husam Nassr.

I would like to express my deepest gratitude to my parents, Mr. Qinghua Han and Ms. Xiufeng Wang, for their unconditional love and support throughout the years. I could have never accomplished this work without them.

TABLE OF CONTENTS

LIST OF ILLUSTRATIONS

LIST OF TABLES

1 INTRODUCTION

1.1 BACKGROUND AND PROBLEM STATEMENT

Modem wireless communication systems are facing the pressing challenges of increasing transmission data rate, reducing cost, reducing transmission power and improving communication reliability. Linear precoding has been considered as one of the promising techniques for achieving these goals. Linear precoding is classified as four categories based on the design methodology [1]:

- Maximize the diversity: A pairwise error probability analysis is applied to maximize the diversity order [2].
- Maximize the capacity: The ergotic or outage capacity is utilized as design criteria for precoder optimization [3, 4].
- Minimize mean squared error (MSE) or maximize signal-to-noise ratio (SNR): The MSE or SNR is used as the merit to design the linear precoder [5].
- Maximize the mutual information: The linear precoder is designed by maximizing the average mutual information of fading channels [12].

The existing linear precoding algorithms commonly assume that the transmitter knows the accurate instantaneous channel state information (CSI). However, practical system often rely on feedback loop to obtain CSI. To verify the effect of the linear precoder designed with inaccurate instantaneous CSI, this dissertation implements an iterative multi-input multi-output orthogonal frequency-division multiplexing (MIMO-OFDM) transceiver. The transmitter incorporates linear precoder designed with instantaneous CSI. The receiver implements MMSE-IC (minimum mean

square error interference cancelation) detector, channel estimator, low-density parity-check (LDPC) decoder and other supporting modules.

A design challenge in turbo receiver is the high computational complexity due to a large number of matrix inversion when the number of subcarriers in the MIMO-OFDM system is on the order of thousands. Matrix inversion is usually implemented by QR decomposition (QRD) followed by back substitution in the hardware. Three known algorithms are widely used for decomposing a matrix into a unitary matrix $\mathbf{Q}$ and an upper triangular matrix $\mathbf{R}$: Gram-Schmidt [5], Householder transformation, and Givens rotation [9]. Givens rotation is advantageous to perform QRD by the CORDIC algorithm in systolic array architecture [7]. However, most works on the QRD implementation consider the system equation of the form $\mathbf{As} = \mathbf{b}$ with $\mathbf{s}$ and $\mathbf{b}$ being single-column variable vector and observation vector, respectively. In the MMSE-IC turbo detection, the received signal is to minus the reconstructed interference from the detected symbols of the previous iteration. Consequently, for each equivalent subcarrier, the MMSE-IC has to solve a set of linear system equations of the form $\mathbf{AX} = \mathbf{B}$, where matrix $\mathbf{A}$ is the channel Gram matrix plus the noise covariance matrix, each column of matrix $\mathbf{B}$ contains the observation vector with interference-canceled for the corresponding symbol, and the diagonal elements of matrix $\mathbf{X}$ are the symbols to be detected. This imposes more computational complexity and latency than that with no interference cancelation. This dissertation proposes an iterative MIMO-OFDM receiver using a new 4-CORDIC QRD for the MMSE-IC algorithm and implements a complete baseband turbo receiver in Field Programmable Gate Array (FPGA).

The instantaneous CSI varies very fast in the practice system and the feedback instantaneous CSI in the transmitter may be outdated. Therefore, the precoding algorithms based on slowly varied statistic CSI were studied [12]. The foundation of the algorithms is the Kronecker model. That is the channel correlation matrix

can be separated into the Kronecker product of the transmit and receive spatial correlation. However, a number of field measurements and simulation analyses have found that the separable Kronecker model is often inaccurate [24, 25]. To validate the accuracy of the Kronecker model, this dissertation performs a experimental channel-sounding campaign based on 4×4 MIMO wideband fading channels measured in both indoor and outdoor environments. A higher-rank principle Kronecker model (PKM) decomposed using the higher-order singular value decomposition (HOSVD) method is also proposed, which has higher accuracy than commonly-used Kronecker model.

1.2 SUMMARY OF CONTRIBUTIONS

This dissertation consists of a couple of journal publications and conference papers as listed in the publication list. My contributions that are published or under review are:

1. This dissertation proposes an implementation of an iterative MIMO-OFDM receiver including MMSE-IC detector, channel estimator, LDPC decoder and other supporting modules. In the MMSE-IC detector, a new 4-CORDIC QRD is proposed. Only four CORDIC cores are applied to compute the Givens rotation coefficients by exploring the property of the equivalent channel matrix. The multipliers are used to rotate multiple columns of matrices **A** and **B** instead of the systolic array. The MMSE-IC detector can be configured as 16-matrix or 64-matrix pipelining with different numbers of multipliers to achieve two different throughput. 1-D and 2-D array for back substitution are proposed to be combined with the two 4-CORDIC QRD schemes. The two schemes for MMSE-IC detector have been implemented on Field Programmable Gate Array (FPGA) for a baseband receiver of equivalent 4×4 MIMO with 1024 subcarrier OFDM. Their resource usage, throughput, and latency are compared with two classic systolic array architectures. The results demonstrate that the

proposed 4-CORDIC QRD schemes achieve the best tradeoff between throughput and resource usage.

2. A higher-rank PKM is proposed for simulating triply-selective fading channels. To construct the PKM, the channel correlation matrices are decomposed using the HOSVD method. The proposed PKM-HOSVD model improves upon the original Kronecker model by using higher-rank approximation of the channel correlation matrices rather than the rank-1 approximation. The proposed PKM-HOSVD is validated by an experimental channel-sounding campaign. In the measurement, a 4×4 MIMO wideband system are built. The measurement is conducted in both indoor and outdoor environments. The carrier frequencies in the experiment are 800 MHz, 2.2 GHz, and 5.2 GHz, respectively. Both the correlation matrix distance (CMD) metric and mean square error (MSE) are applied to evaluate the decomposition's accuracy. The results confirm that many practical channels must use higher-rank approximation rather than the commonly-used rank-1 approximation (or the Kermoal method) to achieve satisfactory decomposition accuracy. This dissertation also propose that the rank-1 Kronecker model always underestimate the channel capacity but the PKM-HOSVD model can predict the channel capacity accurately by choosing different ranks. Finally, the dissertation verify that the CMD can be used to evaluate accuracy of the capacity prediction.

1.3 REFERENCES

[1] C. Xiao, Y. R. Zheng, and Z. Ding, "Globally optimal linear precoders for finite alphabet signals over complex vector Gaussian channels," *IEEE Trans. on Signal Process.*, vol. 59, pp. 3301-3314, July 2011.

[2] Y. Xin, Z. Wang, and G. B. Giannakis, "Space-time diversity systems based on linear constellation precoding," *IEEE Trans. Wireless Commun.*, vol. 2, pp. 294-309, Mar. 2003.

[3] T. M. Cover and J. A. Thomas, *Elements of Information Theory*, 2nd ed. New York: Wiley, 2006.

[4] A. Goldsmith, S. A. Jafar, N. Jindal, and S. Vishwanath, "Capacity limits of MIMO channels", *IEEE J. Seleted. Areas Commun.*, vol.21, pp. 684-702, Jun. 2003.

[5] D. P. Palomar, J. Cioffi and M. A. Lagunas, "Joint Tx-Rx beamforming design for multicarrier MIMO channels: A unified framework for convex optimization," *IEEE Trans. Signal Process.*, vol. 51, pp.2381-2401, Sep 2003.

[6] W. Zeng, C. Xiao, M. Wang, and J. Lu, "Linear precoding for finite-alphabet inputs over MIMO fading channels with statistical CSI," *IEEE Trans. Signal Process.*, vol. 60, no. 6, pp. 3134–3148, Jun. 2012.

[7] M. Tuchler, R. Koetter, and A. Singer, "Turbo equalization: principles and new results," *IEEE Trans. Commun.*, vol. 50, no. 5, pp. 754–767, May 2002.

[8] L. Boher, R. Rabineau, and M. Helard, "FPGA implementation of an iterative receiver for MIMO-OFDM systems," *IEEE J. Sel. Areas Commun.*, vol. 26, no. 6, pp. 857–866, Aug. 2008.

[9] R.-H. Chang, C.-H. Lin, K.-H. Lin, C.-L. Huang, and F.-C. Chen, "Iterative QR decomposition architecture using the modified gram-schmidt algorithm for MIMO systems," *IEEE Trans. Circuits Syst. I, Reg. Papers*, vol. 57, no. 5, pp. 1095–1102, May 2010.

[10] Z.-Y. Huang and P.-Y. Tsai, "Efficient implementation of QR decomposition for gigabit MIMO-OFDM systems," *IEEE Trans. Circuits Syst. I, Reg. Papers*, vol. 58, no. 10, pp. 2531–2542, Oct. 2011.

[11] H. Ozcelik, M. Herdin, W. Weichselberger, J. Wallace, and E. Bonek, "Deficiencies of 'Kronecker' MIMO radio channel model," *Electron. Lett.*, vol. 39, no. 16, pp. 1209–1210, 2003.

[12] W. Weichselberger, M. Herdin, H. Ozcelik, and E. Bonek, "A stochastic MIMO channel model with joint correlation of both link ends," *IEEE Trans. Wireless Commun.*, vol. 5, no. 1, pp. 90–100, Jan. 2006.

PAPER

I. EFFICIENT IMPLEMENTATION OF AN ITERATIVE MIMO-OFDM RECEIVER USING MMSE INTERFERENCE CANCELATION

Bing Han, Zengli Yang and Yahong Rosa Zheng, *Senior Member, IEEE*

ABSTRACT—An efficient hardware implementation scheme is proposed for iterative multi-input multi-output orthogonal frequency-division multiplexing (MIMO-OFDM) receiver which includes MMSE-IC (minimum mean square error interference cancelation) detector, channel estimator, low-density parity-check (LDPC) decoder and other supporting modules. The proposed implementation uses QR decomposition (QRD) of complex-valued matrices with four co-ordinate rotation digital computer (CORDIC) cores and back substitution to solve the MMSE-IC equations while existing systolic array architectures require 15 to 38 CORDIC cores to achieve similar throughput. The proposed 4-CORDIC QRD architecture can be configured as 16-matrix or 64-matrix pipelining using different numbers of multipliers combining with 1-D or 2-D arrays of back substitution, respectively. The channel estimator implements a commonly-used frequency domain least square (LS) channel estimation with the canonic-signed-digits (CSD) method, thanks to the character of the Zadroff-Chu (ZC) sequence used as the pilot. In the LDPC decoder, the min-sum algorithm is implemented for Quasi-Cyclic LDPC (QC-LDPC) decoding. The two schemes for MMSE-IC detector with different throughput and resource usages have been implemented in Field Programmable Gate Array (FPGA) for a complete baseband turbo receiver. Their resource usages, throughput and latencies are compared with classic systolic array architectures, which demonstrate that the proposed receiver architecture achieves the best tradeoff between throughput and resource usage.

ACKNOWLEDGEMENT

We thank Drs. Chengshan Xiao and Zhaocheng Wang for their helpful advices during the development of the work. Part of the hardware implementation was done by Drs. Huang Lou and Mingxi Wang, who were members of the project team.

1 INTRODUCTION

Multiple-input multiple-output (MIMO) orthogonal frequency-division multiplexing (OFDM) techniques has been widely used in recent wireless communication systems and standards [1]. To combat co-channel interference (CCI) inherent in MIMO systems, turbo iterative detector is often required to achieve high performance. Turbo MIMO detection is similar to the turbo equalizers proposed for multipath channels to combat inter-symbol interference (ISI) [3, 4]. The minimum mean square error (MMSE) turbo linear equalizer with interference cancelation (MMSE-IC) [4, 7] is shown to achieve good tradeoff between computational complexity and bit-error-rate (BER) performance.

A general MMSE-IC receiver usually includes the channel estimator, MMSE-IC detector, decoder and other supporting modules. A design challenge in turbo iterative receiver is the increased computational complexity because matrix inversion is required to solve a large set of system equations. For example, for a 2×2 MIMO with 2048 subcarriers employing precoder and 2-subcarrier grouping, the turbo receiver has to perform matrix inversion for the 1024 equivalent channel matrices of size 4×4. Additionally, with MMSE-IC turbo detection, the received signal is to minus the reconstructed interference from the detected symbols of the previous iteration. Consequently, for each equivalent subcarrier, the MMSE-IC has to solve a set of linear system equations of the form $\mathbf{AX} = \mathbf{B}$, where matrix $\mathbf{A}$ is the channel Gram matrix plus the noise covariance matrix, each column of matrix $\mathbf{B}$ contains the observation vector with interference-canceled for the corresponding symbol, and the diagonal elements of matrix $\mathbf{X}$ are the symbols to be detected. This imposes more computational complexity and latency than that with no interference cancelation.

In hardware implementation, matrix inversion is usually accomplished by QR decomposition (QRD) followed by back substitution. Commonly used QR decomposition algorithms include Gram-Schmidt [5], Householder transformation, and Givens rotation [9]. With the co-ordinate rotation digital computer (CORDIC) cores widely available [7], Givens rotation is adopted in many recent works with the systolic array architecture [7, 9]. However, most works on the QRD implementation consider the system equation of the form $\mathbf{As} = \mathbf{b}$ with $\mathbf{s}$ and $\mathbf{b}$ being single-column variable vector and observation vector, respectively. To apply the conventional QRD for MMSE-IC turbo detection, the Givens rotations of each channel matrix have to be applied to multiple observation vectors in $\mathbf{B}$. Additionally, back substitution has also to be performed for the multiple vectors in $\mathbf{X}$. The systolic array implementation will have to either increase the number of internal cells for parallel rotation of multiple observation vectors, or reuse the array for one-column rotation multiple times to perform the MMSE-IC turbo detection. This means either largely increased resource usage or greatly reduced throughput.

In this paper, we propose an implementation of an iterative MIMO-OFDM receiver including MMSE-IC detector, channel estimator, LDPC decoder and other supporting modules. In the MMSE-IC detector, a new 4-CORDIC QRD is proposed. The proposed QRD scheme explores the property of the equivalent channel matrix so that the Givens rotation coefficients are computed by only four CORDIC cores. Givens rotation for multiple columns of matrices $\mathbf{A}$ and $\mathbf{B}$ is implemented by multipliers without using the systolic array. Taking advantage of the latency of CORDIC cores, the proposed 4-CORDIC QRD is configured as 16-matrix or 64-matrix pipelining with different numbers of multipliers to achieve two different throughput. The two 4-CORDIC QRD schemes are then combined with 1-D or 2-D array for back substitution, respectively. The channel estimator implements a commonly-used frequency domain least square (LS) channel estimation [8] with the canonic-signed-digits

(CSD) method, thanks to the character of the Zadroff-Chu (ZC) sequence used as the pilot. In the LDPC decoder, the min-sum algorithm is implemented for Quasi-Cyclic LDPC (QC-LDPC) decoding [9]. The two schemes for MMSE-IC detector have been implemented on Field Programmable Gate Array (FPGA) for a baseband receiver of equivalent 4×4 MIMO with 1024 subcarrier OFDM. Their resource usage, throughput, and latency are compared with two classic systolic array architectures. The results demonstrate that the proposed 4-CORDIC QRD schemes achieve the best tradeoff between throughput and resource usage.

2 TURBO MMSE DETECTION WITH INTERFERENCE CANCELATION

Consider a MIMO-OFDM system with N_t transmit antennas, N_r receive antennas, and K_c subcarriers. The block diagram of transmitter is shown in Fig. 2.1(a). With linear precoding and/or subcarrier grouping [8], every K_G subcarriers are grouped together and the MIMO-OFDM channel is equivalent to K_c/K_G subcarriers with $M \times N$ MIMO, where $M = N_r \cdot K_G$ and $N = N_t \cdot K_G$. Figure 2.2 shows two conventional frame structures for $N_t = 2$, where two pilot blocks are used for channel estimation. In frame structure 1, the pilot and data blocks are transmitted separately and with their own cyclic prefix (CP); In frame structure 2, the pilot and data blocks are transmitted together with one common CP block. The frame length is determined by channel variation and we assume the channel estimation is only performed with pilot blocks and remains unchanged within each frame.

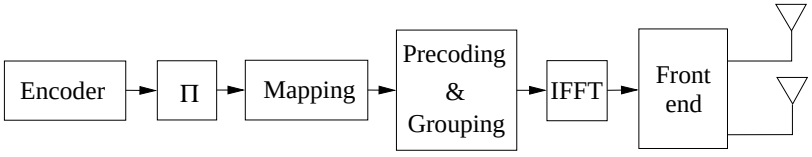

(a) Transmitter.

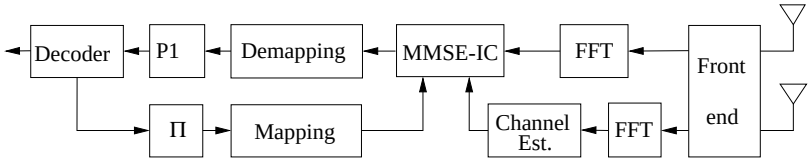

(b) Receiver.

Figure 2.1. The block diagram of the MMSE-IC transceiver, where Π is the interleaver and Π^{-1} is the de-interleaver.

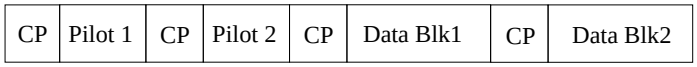

(a) Frame structure 1.

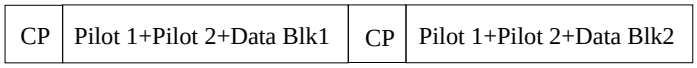

(b) Frame structure 2.

Figure 2.2. Two signal structures, where CP = cyclic prefix.

The MMSE-IC turbo detector for frame structure 1 is shown in Fig. 2.2, where the front end processes the received signals and outputs baseband I and Q signals and removes the CPs. The pilot blocks are obtained first and used for channel estimation yielding the frequency domain channel coefficients. The data blocks are converted to frequency domain via fast fourier transform (FFT). Soft symbol LLRs are exchanged between the MMSE-IC MIMO detector and the channel decoder for turbo detection. In the receiver with frame structure 2, the pilot and data blocks are obtained after one FFT module at the same time.

Let $\mathbf{y_k} \in \mathbb{C}^{M\times 1}$ and $\mathbf{H}_{e,k} \in \mathbb{C}^{M\times N}$ denote the received vector and the equivalent channel matrix of the k-th sub-channel, respectively. We have

$$\mathbf{y}_k = \mathbf{H}_{e,k}\mathbf{s}_k + \mathbf{v}_k, \qquad k = 1, 2, ..., K_c/K_G, \tag{1}$$

where $\mathbf{s}_k \in \mathbb{C}^{N\times 1}$ is the transmitted symbol vector and $\mathbf{v}_k \in \mathbb{C}^{M\times 1}$ is the noise vector with power σ_v^2. In the first iteration, no prior LLR is available, thus the MMSE-IC computes the estimate of the symbol vector by

$$\hat{\mathbf{s}}_k = (\mathbf{H}^{\dagger}_{\mathbf{e,k}}\mathbf{H}_{\mathbf{e,k}} + \sigma^{\mathbf{2}}_{\mathbf{v}}\mathbf{I})^{-\mathbf{1}}\mathbf{H}^{\dagger}_{\mathbf{e,k}}\mathbf{y_k}, \tag{2}$$

where superscript † denotes the Hermitian transpose. Solving (2) is usually accomplished by solving the linear system equation [7] as

$$\mathbf{A}\hat{\mathbf{s}}_k = \mathbf{b}, \tag{3}$$

where $\mathbf{A} = \mathbf{H}_{\mathbf{e,k}}^{\dagger}\mathbf{H}_{\mathbf{e,k}} + \sigma_{\mathbf{v}}^{\mathbf{2}}\mathbf{I}$ and $\mathbf{b} = \mathbf{H}_{e,k}^{\dagger}\mathbf{y_k}$.

In the second and subsequent iterations, the MMSE-IC detector reconstructs the interference by

$$\mathbf{y}'_{\mathbf{k,n}} = \mathbf{y_k} - \mathbf{H}_{\mathbf{e,k}}\tilde{\mathbf{s}}_{\mathbf{k,n}}, \tag{4}$$

where $\tilde{\mathbf{s}}_{k,n} = [\hat{s}_{k,1}, ..., \hat{s}_{k,n-1}, 0, \hat{s}_{k,n+1}, ..., \hat{s}_{k,N}]$ with $\hat{s}_{k,n}$ being the estimated symbols from the previous iteration. Then the MMSE-IC detector computes the n-th symbol of the k-th subcarrier by

$$\hat{s}_{k,n} = \mathbf{e_n}(\mathbf{H}_{\mathbf{e,k}}^{\dagger}\mathbf{H}_{\mathbf{e,k}} + \sigma_{\mathbf{v}}^{\mathbf{2}}\mathbf{I})^{-\mathbf{1}}\mathbf{H}_{\mathbf{e,k}}^{\dagger}\mathbf{y}'_{\mathbf{k,n}}, \quad \mathbf{n} = \mathbf{1}, \mathbf{2}, ..., \mathbf{N}, \tag{5}$$

where $\mathbf{e_n}$ is a $1 \times N$ vector with all elements equal to 0 except the n-th element that is equal to 1.

Equation (5) can also be viewed as the solution to a set of linear system equations:

$$\mathbf{AX} = \mathbf{B}, \tag{6}$$

where $\mathbf{X} = \mathrm{diag}(\hat{\mathbf{s}}_k)$, and the n-th column of $\mathbf{B}$ is $\mathbf{H}_{e,k}^{\dagger}\mathbf{y}'_{\mathbf{k,n}}$.

It is well known that QRD and back substitution are used to solve the linear system equations (3) and (6). Consider a 4×4 complex matrix $\mathbf{A} = \{a_{mn}\}$ for $m = 1, ..., 4$ and $n = 1, ..., 4$. A Givens rotation matrix $\mathbf{G_1}$ that cancels a_{21} by a_{11} is

given by

$$\mathbf{G}_1 = \begin{bmatrix} C_1 & S_1 & 0 & 0 \\ -S_1^{\dagger} & C_1^{\dagger} & 0 & 0 \\ 0 & 0 & 1 & 0 \\ 0 & 0 & 0 & 1 \end{bmatrix}, \tag{7}$$

where, using the famous CORDIC algorithm,

$$\begin{aligned} C_1 &= \cos(\theta_1) e^{-\iota\phi_1}, \\ S_1 &= \sin(\theta_1) e^{-\iota\varphi_1}, \end{aligned} \tag{8}$$

where $\tan(\theta_1) = |a_{21}| \,/\, |a_{11}|$; ϕ_1 and φ_1 are the phases of a_{11} and a_{21}, respectively; ι denotes $\sqrt{-1}$. Thus,

$$\mathbf{G}_1\mathbf{A} = \begin{bmatrix} a_{11}^{(1)} & a_{12}^{(1)} & a_{13}^{(1)} & a_{14}^{(1)} \\ 0 & a_{22}^{(1)} & a_{23}^{(1)} & a_{24}^{(1)} \\ a_{31} & a_{32} & a_{33} & a_{34} \\ a_{41} & a_{42} & a_{43} & a_{44} \end{bmatrix}, \tag{9}$$

where the superscript represents the count of rotations, $a_{11}^{(1)}$ becomes a real positive number, and the updated elements in the first two rows become:

$$\begin{aligned} a_{1n}^{(1)} &= C_1 a_{1n} + S_1 a_{2n}, \\ a_{2n}^{(1)} &= -S_1^{\dagger} a_{1n} + C_1^{\dagger} a_{2n}. \end{aligned} \tag{10}$$

After the QRD, we obtain

$$\mathbf{R}\mathbf{X} = \mathbf{Q}^{\dagger}\mathbf{B} = \mathbf{Z}. \tag{11}$$

where $\mathbf{Q}^{\dagger} = \mathbf{G}_6\mathbf{G}_5\mathbf{G}_4\mathbf{G}_3\mathbf{G}_2\mathbf{G}_1$, and

$$\mathbf{R}= \begin{bmatrix} a_{11}^{(3)} & a_{12}^{(3)} & a_{13}^{(3)} & a_{14}^{(3)} \\ 0 & a_{22}^{(5)} & a_{23}^{(5)} & a_{24}^{(5)} \\ 0 & 0 & a_{33}^{(6)} & a_{34}^{(6)} \\ 0 & 0 & 0 & a_{44}^{(6)} \end{bmatrix}. \tag{12}$$

The solution to $\mathbf{X}$ is then obtained by back substitution column by column.

To solve (6), the Givens rotation has to be performed on all N columns of $\mathbf{B}$ and the back substitution is also performed for each column of $\mathbf{X}$. This increases the computational complexity of MMSE-IC turbo detector over ordinary MMSE turbo detector.

A common implementation of QRD is to use the systolic array architecture [10,11], where the boundary cells operate in the vectoring mode and the internal cells operate in the rotation mode. Each boundary cell uses two CORDIC cores for complex vectoring mode, and each internal cell uses three CORDIC cores for complex rotation mode. If the rotation of the columns of $\mathbf{B}$ is implemented by one column of internal cells, then the systolic array uses a total of 38 CORDIC cores for the QRD of a 4×4 complex matrix. The systolic array rotates one column of $\mathbf{B}$ at a time by reusing the same systolic array multiple times, thus reducing the throughput of the MMSE-IC detector. We call this scheme SA-QRD-I. On the other hand, if more internal cells are added to rotate all columns of $\mathbf{B}$ simultaneously, then the throughput can be four times as that of the SA-QRD-I scheme, but the cost is 74 CORDIC cores. We call this scheme SA-QRD-II. Although some recent works [7,9] manage to reduce the number of CORDIC cores by modifying the conventional systolic array architecture, the number of the cores required is still as high as 15 to 38 for the QRD of each 4×4 matrix.

3 THE PROPOSED MMSE TURBO DETECTOR USING 4-CORDIC QRD AND BACK SUBSTITUTION

In this section, we propose an alternative approach to implementing the MMSE-IC turbo detector without using systolic array for QRD. We use only four CORDIC cores and some complex-valued multipliers to implement the Givens rotation directly. This is motivated by the fact that for each k a common QRD of matrix $\mathbf{A}$ is used for all column rotations in each MMSE-IC iteration. Besides, for the signal frame structure shown in Fig. 2.1, the channel matrices of all subcarriers are available way ahead of the received data symbols and remain unchanged within the data frame. Therefore, the QRD can be performed before the arrival of the data signals and be saved for later use with all data blocks. This approach relaxes the throughput and timing requirements of the QRD.

To illustrate our proposed approach, we focus on solving the system equations (6) since (3) is a special case of (6). To separate the channel matrix from the data vectors, we modify the matrix $\mathbf{B}$ as $\mathbf{B}_H = \mathbf{H}_{e,k}^{\dagger}$, and our purpose is to solve

$$\mathbf{A}\mathbf{X}_H = \mathbf{B}_H. \tag{13}$$

and obtain

$$\mathbf{R}\mathbf{X}_H = \mathbf{Z}_H, \tag{14}$$

where $\mathbf{Z}_H = \mathbf{Q}^{\dagger}\mathbf{B}_H$ and $\mathbf{X}_H = (\mathbf{H}_{e,k}^{\dagger}\mathbf{H}_{e,k} + \sigma_v^2\mathbf{I})^{-1}\mathbf{H}_{e,k}^{\dagger}$. Let $\mathbf{X}_H = \{x_{mn}\}$ and $\mathbf{Z}_H = \{z_{mn}\}$ for $m = 1, ..., N$ and $n = 1, ..., N$. The solution is obtained by back substitution

$$x_{mn} = \frac{1}{r_{mm}}\left(z_{mn} - \sum_{p=m+1}^{N} r_{mp}x_{pn}\right). \tag{15}$$

When the data block is available, we multiple the n-th row of $\mathbf{X}_H$ with $\mathbf{y'_{k,n}}$ to yield the n-th soft symbol

$$\hat{s}_{k,n} = [x_{n1}, x_{n2}, ..., x_{nN}] \cdot \mathbf{y'_{k,n}}, \qquad \mathbf{n} = \mathbf{1}, ..., \mathbf{N}. \tag{16}$$

Figure 3.1 shows the block diagram of the proposed MMSE-IC turbo detector. The blocks M_MUL, M_ADD and M_SUB denote the matrix multiplication, addition, and subtraction, respectively. The extrinsic information of the MMSE-IC turbo detector $\hat{\mathbf{s}}$ is interleaved and sent to the low-density parity-check (LDPC) decoder as its *a priori* input. The LDPC decoder computes the extrinsic information as the output, which is fed back to the MIMO detector as the *a priori* information $\tilde{\mathbf{s}}$. After multiple turbo iterations, hard decisions are made at the output of the LDPC decoder. Since the LDPC decoder is resource intensive, the LDPC_p2s and LDPC_s2p modules are used here to decode multiple LDPC code blocks in serial. If high throughput is desired, then the parallel to serial conversion shall be removed and multiple LDPC decoders shall be instantiated.

For frame structure 2 in Fig. 2.2(b) the proposed MMSE-IC turbo detector is also applicable. Although the pilot and data blocks are available at the same time, the channel matrices remain unchanged at every iteration. Therefore, we also separate the channel matrix from the data vectors and modify $\mathbf{B}$ as $\mathbf{B}_H$. The QRD and back substitution will be performed once for each subcarrier in every data frame. The solution $\mathbf{X}_H$ is multiplied with updated $\mathbf{y'_{k,n}}$ at every iteration.

3.1 THE 4-CORDIC QRD FOR MMSE-IC TURBO DETECTOR

An observation on the MMSE-IC detector is that matrix $\mathbf{A}$ is positive semi-definite and its diagonal elements are all real. If a_{mm} is used to zero the elements a_{nm} with $n > m$, then a_{mm} remains real through the m-th column zeroing. The

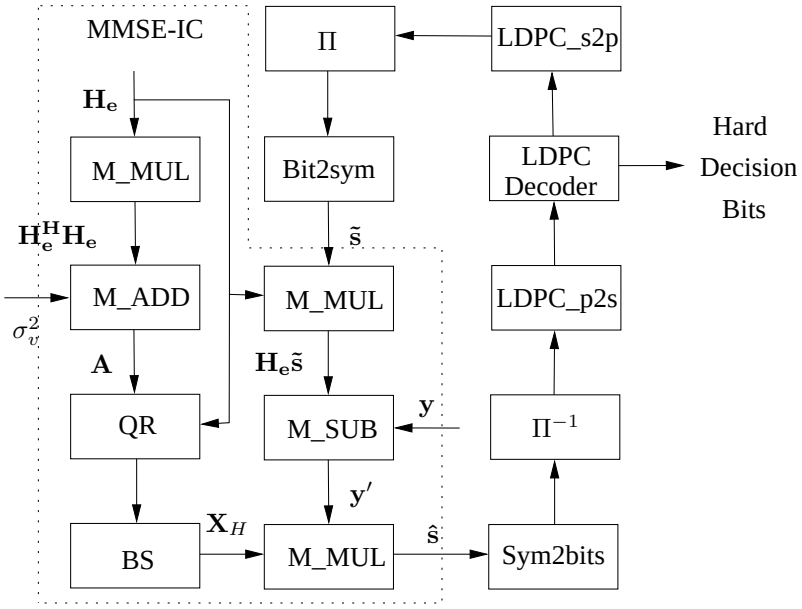

Figure 3.1. Block diagram of the implemented MMSE-IC turbo detector.

verification of this property is omitted in the paper. This observation helps to save two CORDIC cores in our proposed QRD architecture.

The block diagram of the proposed QRD is shown in Fig. 3.2, where the first rotation is depicted as an example. The first input to the QRD module (denoted as QR_SUB) is always the diagonal element of $\mathbf{A}$ and is always real. That is $\phi_1 = 0$ or π in (8). Therefore, its sign and amplitude are easily obtained via the absolute value module ABS. The second input to QR_SUB is a complex element a_{21}, and CORDIC 1, operating in the vectoring mode, computes the amplitude $|a_{21}|$ and phase φ_1. The amplitudes $|a_{11}|$ and $|a_{21}|$ are fed to CORDIC 2. Also set in the vectoring mode, CORDIC 2 outputs the phase θ_1 and the amplitude $a_{11}^{(1)} = \sqrt{|a_{11}|^2 + |a_{21}|^2}$, which are, respectively, the input to CORDIC 3 and the input to the ABS of the next rotation. CORDIC 3 takes the input θ_1 and operates in the rotation mode to yield $\cos(\theta_1)$ and $\sin(\theta_1)$. The SEL block takes the sign of a_{11} and flips the sign of $\cos(\theta_1)$ if $\text{sign}(a_{11}) < 0$, yielding the rotation coefficient $C_1 = \text{sign}(a_{11})\cos(\theta_1)$. The NEG block

changes the sign of φ_1 and outputs to CORDIC 4. Operating in the rotation mode, CORDIC 4 computes $S_1 = \sin(\theta_1)e^{-\iota\varphi_1}$. Due to the latency of the CORDIC cores, the 4-CORDIC architecture exhibits 83 clock cycles of delay which can be exploited for pipelining.

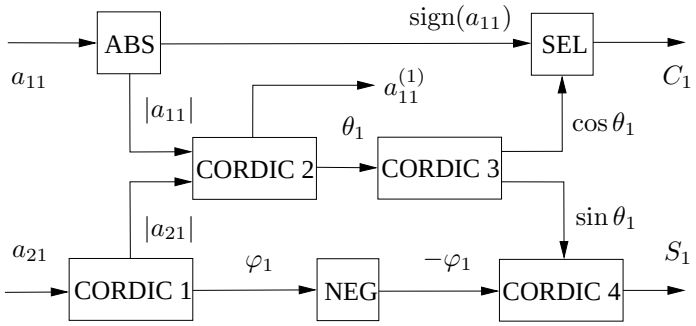

Figure 3.2. The block diagram of QR_SUB module.

Then we use the module named QR_MUL to rotate the remaining elements in the first two rows of $\mathbf{A}$ and the corresponding elements of $\mathbf{B}_H$. Since C_1 is real, (10) is implemented as

$$\begin{aligned}
\text{real}(a_{1n}^{(1)}) &= C_1 \cdot \text{real}(a_{1n}) + \text{real}(S_1) \cdot \text{real}(a_{2n}) - \text{imag}(S_1) \cdot \text{imag}(a_{2n}), \\
\text{imag}(a_{1n}^{(1)}) &= C_1 \cdot \text{imag}(a_{1n}) + \text{real}(S_1) \cdot \text{imag}(a_{2n}) + \text{imag}(S_1) \cdot \text{real}(a_{2n}), \\
\text{real}(a_{2n}^{(1)}) &= C_1 \cdot \text{real}(a_{2n}) - \text{real}(S_1) \cdot \text{real}(a_{1n}) - \text{imag}(S_1) \cdot \text{imag}(a_{1n}), \\
\text{imag}(a_{2n}^{(1)}) &= C_1 \cdot \text{imag}(a_{2n}) - \text{real}(S_1) \cdot \text{imag}(a_{1n}) + \text{imag}(S_1) \cdot \text{real}(a_{1n}),
\end{aligned} \tag{17}$$

where $n = 2, 3, 4$, real() and imag() denote the real and imaginary part of a complex number, respectively. It is clear from (17) that the QR_MUL module includes 12 real multipliers. To zero a_{21}, a_{31} and a_{41}, we use three QR_MUL operations. Similarly, the corresponding two rows of matrix $\mathbf{B}_H$ are rotated with four QR_MUL operations.

These QR_MUL operations may be implemented in parallel or serial depending on the pipelining design of the QRD. Since the latency of the 4-CORDIC QRD is 83 clock cycles, two pipelining designs are appropriate. One is a 16-matrix pipelining with two QR_MUL modules operating in serial mode for rotation. Another is a 64-matrix pipelining with seven QR_MUL modules operating in parallel. These two schemes provide two different tradeoff between throughput and resource usage. In frame structure 1 shown in Fig. 2.1, the channel matrices are obtained from the pilot blocks ahead of the received data symbols. Therefore, there is enough time to perform QRD and back substitution before the arrival of the data signals. In this case, throughput requirement is low, thus the 16-matrix pipelining scheme is suitable and can reduce the resource usage. If high throughput is required, then the 64-matrix pipelining can be used at a cost of increased resource usage.

The data flow diagram of the 16-matrix pipelining QRD is shown in Fig. 3.3, where the first rotation is depicted as an example. The input $\mathbf{A}$ and $\mathbf{B}$ matrices are saved in RAM_A and RAM_B, respectively. The QR_SUB module reads a_{11} and a_{21} to compute C_1 and S_1. The MUL_A block includes one QR_MUL module if the 16-matrix pipelining is used. It reads a_{1n} and a_{2n} $(n = 2, 3, 4)$ from RAM_A in series and reuses the one QR_MUL module three times to rotate the top two rows of matrix $\mathbf{A}$. Similarly, the MUL_B contains one QR_MUL module and reuse it four times to rotate the corresponding rows of matrix $\mathbf{B}_H$. The updated elements are saved back in RAM_A and RAM_B, respectively.

The timing control of the 16-matrix pipelining QRD is shown in Fig. 3.4. A finite-state machine (FSM) with seven states is used to control the QRD process of a 4×4 complex matrix. The FSM starts at State 0 and transits to State 1 through State 6 sequentially. At the beginning of State 0, QR_SUB reads 16 pairs of a_{11} and a_{21} in 16 clock cycles. The 4-CORDIC QRD scheme computes C_1 and S_1 for each pair of a_{11} and a_{21} using pipelining. The first $a_{11}^{(1)}$ is available at the 40th clock cycle

and the 16 pairs of $a_{11}^{(1)}$ and a_{31} are pipelined into QR_SUB at the 64th clock cycle. When C_1 and S_1 are available at the 83rd clock cycle, the FSM transits to State 1. In State 1, QR_SUB computes C_2 and S_2, while QR_MUL_A and QR_MUL_B rotate the top two rows of matrices $\mathbf{A}$ and $\mathbf{B}_H$, respectively. There is a two clock cycles delay in the QR_MUL modules. In the first rotation, QR_MUL_A is reused three times for serially rotating the 2nd to 4th columns of each matrix $\mathbf{A}$, as shown in Fig. 3.4(b). Similarly, the QR_MUL_B module is reused four times to rotate the four columns of each matrix $\mathbf{B}_H$. The total time required for State 1 is 64 clock cycles. When rotation of the top two rows of matrix $\mathbf{B}_H$ is completed, the FSM enters State 2. The QR_SUB and QR_MUL modules compute the Givens rotation for the 1st and 3rd rows of matrices $\mathbf{A}$ and $\mathbf{B}_H$. Similarly, State 3 computes the rotation for the 1st and 4th rows of matrices $\mathbf{A}$ and $\mathbf{B}_H$ with similar timing control. State 4, 5, 6 are for $\mathbf{G}_4$, $\mathbf{G}_5$ and $\mathbf{G}_6$, respectively, with similar timing because all QR_MUL_B require 64 clock cycles, although QR_MUL_A has less columns to rotate. In State 6, the resulting $\mathbf{R}$ matrix of the first $\mathbf{A}$ matrix is available at the 429th clock cycles and the rotations of the first $\mathbf{B}_H$ are completed at the 479th clock cycles. The FSM returns to State 0 for the next group of 16 matrices.

For a higher throughput, the QRD is configured as 64-matrix pipelining. The data flow diagram is the same as that in Fig. 3.3. Three QR_MUL modules are instantiated for rotating matrix $\mathbf{A}$. Meanwhile, the rotation of matrix $\mathbf{B}_H$ is performed by another four QR_MUL modules since matrix $\mathbf{B}_H$ always has four elements in each row for rotation. The timing control is achieved by a 7-state FSM similar to the 16-matrix pipelining.

3.2 BACK SUBSTITUTION

Back substitution is often implemented by a 1-D array [8] for the matrix QRD. In this paper, we pipeline the conventional 1-D array [8, Chapter 2] and double the

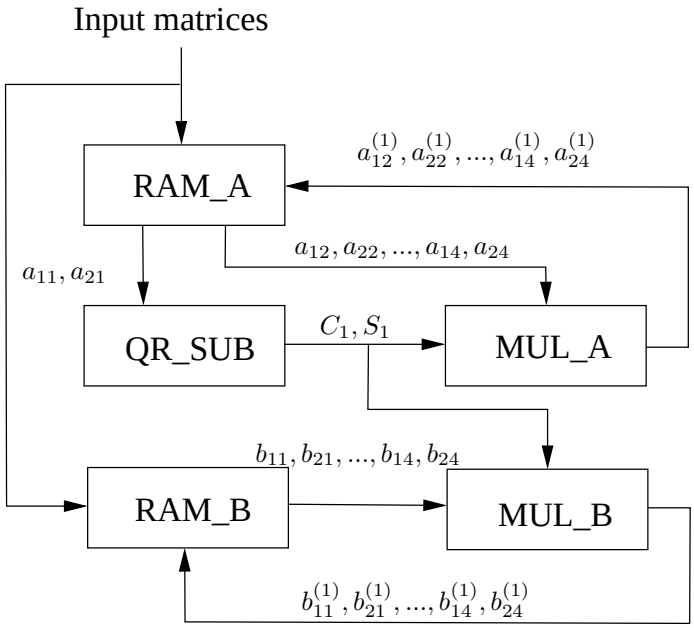

Figure 3.3. Data flow diagram of the proposed QRD scheme.

throughput for the 16-matrix pipelining QRD. The block diagram is shown in Fig. 3.5(a). In each boundary and internal cell, the calculation is finished in one processing cycle which consists of two clock cycles. Initially, let $\{t_{mn}\} = 0$ for $m = 1, ..., N$ and $n = 1, ..., N$. At the 0th processing cycle, r_{44} and z_{41} are fed into the boundary cell and $x_{41} = z_{41}/r_{44}$ is obtained at the output ports. In the next processing cycle, r_{44} and z_{42} are fed into the boundary cell to compute $x_{42} = z_{42}/r_{44}$. Meanwhile, x_{41} and r_{34} are fed into to internal cell 1 to compute $t_{31} = r_{34}x_{41}$. This means two columns of $\mathbf{Z}_H$ and $\mathbf{X}_H$ are pipelined. In the next two processing cycles, $\{r_{33}, z_{31}, t_{31}\}$ and $\{r_{33}, z_{32}, t_{32}\}$ are fed into the boundary cell to compute $x_{31} = (z_{31} - t_{31})/r_{33}$ and $x_{32} = (z_{32} - t_{32})/r_{33}$, respectively. The three internal cells yield the summation function $t_{mn} = \sum_{p=m+1}^{4} r_{mp}x_{pn}$. The solutions to $\mathbf{X}_H$ are obtained from the boundary cell at the 16th processing cycle.

It is worth noting that in the original 1-D array, two clock cycles are required to obtain one element of the solutions or eight clock cycles to solve each column of

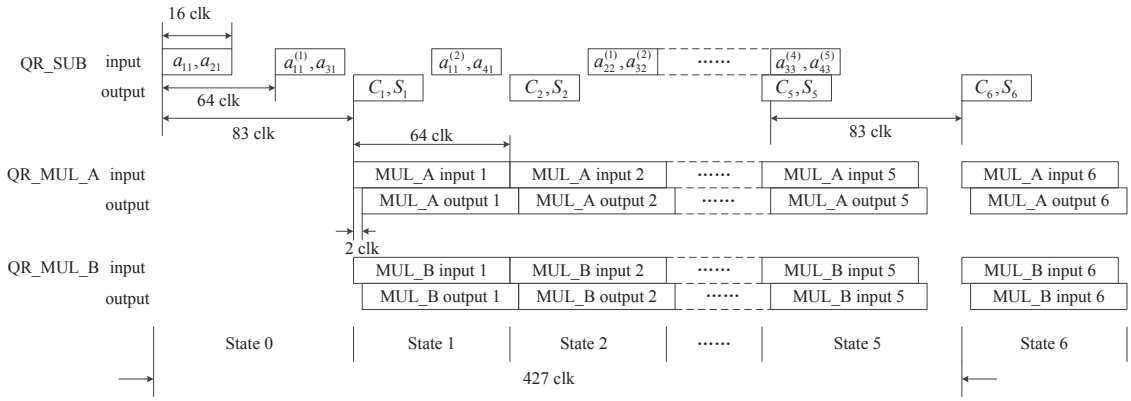

(a) Block diagram of timing control.

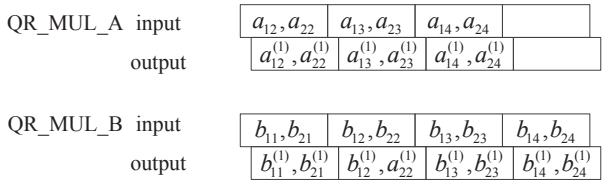

(b) Timing for QR_MUL in the first rotation.

Figure 3.4. Timing control for the proposed 16-matrix pipelining QRD.

$\mathbf{X}_H$, yielding the throughput of 32 clock cycles per $\mathbf{X}_H$. We utilize the timing gap between two elements of the original array and the gap between two processing cycles to implement the 4-column pipelining. The throughput of the proposed 1-D back substitution is four clock cycles per column yielding a throughput of 16 clock cycles per $\mathbf{X}_H$.

Since the 64-matrix pipelining QRD yields a high throughput of seven clock cycles per matrix, we use a 2-D systolic array for back substitution. The block diagram of 2-D back substitution is shown in Fig. 3.5(b), where the first column of the solution is depicted as an example. The numbers in boldface denote the input and output timing in processing cycle count. In 2-D back substitution one processing cycle also consists of two clock cycles. At the 0th processing cycle, boundary cell

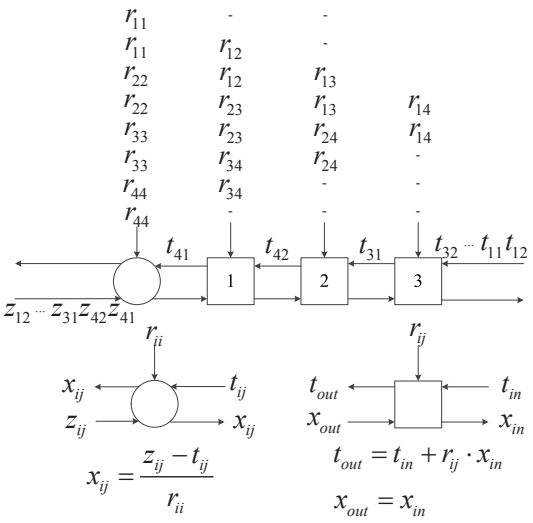

(a) 1-D structure. The boundary cell is complex-valued subtraction and division, and internal cells are complex-valued addition.

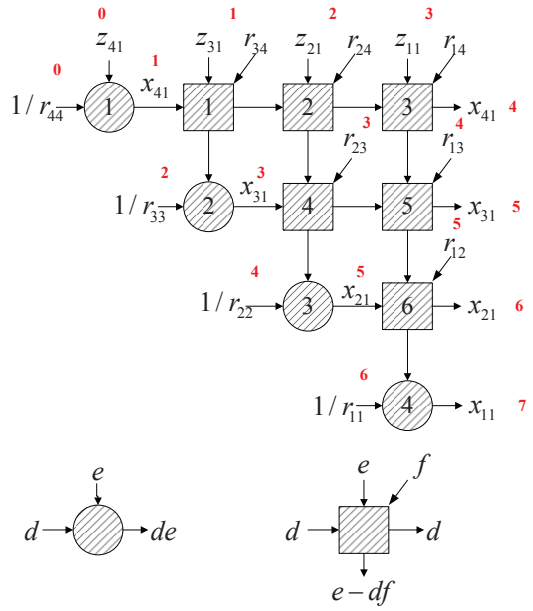

(b) 2-D structure. The boundary cells are multipliers of a real number with a complex number, and internal cells are complex-valued multiplication and subtraction. The numbers in boldface denote the input and output timing in processing cycle count.

Figure 3.5. The systolic arrays for back substitution.

1 outputs $x_{41} = z_{41}/r_{44}$. At the first processing cycle, z_{31}, r_{34} and x_{41} are fed into internal cell 1 to compute $z_{31} - r_{34}x_{41}$. At the 2nd processing cycle, boundary cell 2 outputs $x_{31} = (z_{31} - r_{34}x_{41})/r_{33}$. At the 4th processing cycle, $z_{21} - \sum_{p=3}^{4} r_{2p}x_{p1}$ is fed into boundary cell 3 to compute x_{21}. At the 6th processing cycle, $z_{11} - \sum_{p=2}^{4} r_{1p}x_{p1}$ is fed into boundary cell 4 and x_{11} is obtained at the 7th processing cycle. Similar to 1-D array, the internal cells of the 2-D array perform the summation and the solutions of $\mathbf{X}_H$ are obtained from the boundary cells. In fact the 1-D array is obtained from folding the 2-D array in 45 degrees [13]. Because of the gap between two processing gap, 2-column pipelining is implemented. The throughput of the 2-D back substitution is one clock cycle per column of $\mathbf{X}_H$, resulting in four clock cycles total per $\mathbf{X}_H$ for solving (14).

4 HARDWARE IMPLEMENTATION OF CHANNEL ESTIMATOR AND LDPC DECODER

In this section, the hardware implementations of other supporting modules, such as channel estimator and LDPC decoder, are introduced.

4.1 CHANNEL ESTIMATOR

The frequency domain LS method [8] is used for channel estimation, followed by time-domain truncation. The sequences used for channels estimation are designed as the IFFT of ZC sequence of length K_{chu}, whose k_{chu}-th element [14] is

$$a_{chu}(k_{chu}) = \exp(j\pi \frac{M_{prime}}{K_{chu}}(k_{chu}-1)^2), \quad k_{chu} = 1, 2, ..., K_{chu}. \tag{18}$$

In our design, we choose $K_{chu} = 256$ and $M_{prime} = 1$. The CP sequences are the last 64 samples of $\mathbf{x}_{mn}$.

The received preambles from the n-th receiver are converted to frequency-domain by K_{chu}-point FFT into $\mathbf{Y}_{n1}$ and $\mathbf{Y}_{n2}$. The k_{chu}-th channel tone $H(k_{chu})$ is then estimated as

$$H(k_{chu}) = \frac{1}{2} \begin{bmatrix} Y_{11}(k_{chu}) & Y_{12}(k_{chu}) \\ Y_{21}(k_{chu}) & Y_{22}(k_{chu}) \end{bmatrix} \begin{bmatrix} a^*_{chu}(k_{chu}) & a^*_{chu}(k_{chu}) \\ -a_{chu}(k_{chu}) & a_{chu}(k_{chu}) \end{bmatrix} \tag{19}$$

Note that no matrix inversion is used but matrix multiplication of the Chu sequences. Since the Chu sequences a_{chu} are constants, the matrix multiplication can be efficiently implemented by the CSD method. Then the channel impulse response is obtained by

inverse FFT of the (m, n)-th elements of $\mathbf{H}$. The length of the channel is truncated to a desired channel length that is much smaller than K_{chu}.

4.2 LDPC DECODER

We use the Quasi-Cyclic LDPC (QC-LDPC) code with 3/4 coding rate. The input information bit length is $K_L = 1530$, and the output code length is $N_L = 2040$. The QC-LDPC encoder uses the Richardson-Urbanke (RU) algorithm [15] by row-column permutations of the parity check matrix into an approximate lower triangular matrix. In the decoder, we use the improved semi-parallel decoding architecture [9] consisting of horizontal processing units (HPUs), vertical processing units (VPUs) and three rams: one is used to store check-node message; one is used to store bit-node message; one is used to store the LLRs.

4.3 SYM2BITS AND BIT2SYM BLOCK

In the Sym2bits block, the equalized soft symbols are mapped into bit LLR values for LDPC decoder. The bit LLR is calculated by log-sum-exp functions for each subcarrier k and each bit j of each symbol i. In our implementation, we used the minimum function [16]

$$\ln(\exp(-x) + \exp(-y)) \approx -\min(x, y). \tag{20}$$

to simplify the operation. The percentage error is used as a metric to evaluate the approximate function, which is defined as

$$e = \frac{|\text{Approximate Value} - \text{Exact Value}|}{|\text{Exact Value}|} \times 100\%. \tag{21}$$

The percentage error of the approximation in (20) is shown in Fig. 4.1(a). When $|x-y|$ is large than 3, which is the case of 99.33 % of the time, the percentage error is less than 10.81 %.

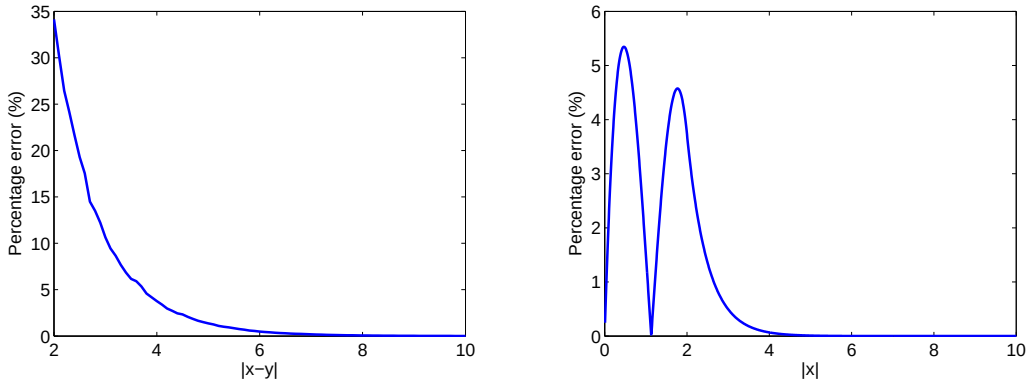

(a) The percentage error of the approximation of $\ln(\exp(-x)+\exp(-y))$ using $-\min(x,y)$. When $|x-y|$ is large than 3, which is the case of 99.33 % of the time, the percentage error is less than 10.81 %.

(b) The percentage error of the sigmoid-like function. The maximal percentage error is 5.35%.

Figure 4.1. The percentage error of the approximation.

In the Bit2sym block, the bit LLRs from LDPC decoder are mapped into soft symbols for MMSE equalization using

$$\tilde{s}_k = \sum_i \alpha_i \prod_j \frac{1}{2}\left[1+\tilde{\beta}_{i,j}\tanh\left(\frac{L(k,j)}{2}\right)\right]. \tag{22}$$

In our implementation, the tanh function is approximated by a sigmoid-like function [17] given by

$$G(x) = \begin{cases} -1, \ x < -\epsilon \\ x(\gamma + \lambda x), \ -\epsilon \leq x \leq 0 \\ x(\gamma - \lambda x), \ 0 \leq x \leq \epsilon \\ 1, \ x > \epsilon \end{cases} \tag{23}$$

where the three constants ϵ, γ and λ are selected as $\epsilon = 4$, $\gamma = 2/\epsilon$ and $\lambda = 1/\epsilon^2$, respectively. The multiplication in (23) is implemented by the CSD method. The percentage error of the sigmoid-like function is shown in Fig. 4.1(b). The maximal percentage error is 5.35%.

5 SIMULATION AND SYNTHESIS RESULTS

To examine the performance of the proposed QRD and back substitution, a 2×2 MIMO 2048-subcarrier OFDM system was built [8] with 2-subcarrier grouping. The data blocks at the transmitter were generated by two raw source bit streams encoded by a length-2040 LDPC encoder with 3/4 coding rate. After LDPC encoding, each codeword was added eight zero bits at the end to form a data block of length 2048, which was then interleaved and modulated to QPSK, 8PSK or 16QAM symbols. After precoding, the symbols of each stream were fed into a subcarrier grouper. Then, each data block was converted to time domain by 2048-point inverse fast Fourier transform (IFFT), followed by CP insertion. A digital up convertor (DUC) was used to up-sample the baseband I/Q signals and modulate them onto IF (intermediate frequency) of 17.5 MHz. The output of the DUC module was fed into the digital to analog converter (DAC) directly and a RF up convertor was used to transmit the signal at 915 MHz. The receivers with the two proposed MMSE-IC turbo schemes were also implemented, in combination with digital down convertors, channel estimator, and LDPC soft decoders.

In the simulation, the experimental 2×2 multi-path channels were used, and the channel impulse response and frequency impulse response are shown in Fig. 5.1(a) and Fig. 5.1(b), respectively. The multi-path channel length was set to 20 taps and the frequency response of the sub-channels has clear nulls. This is typical in the experiments. The BER performance in the SNR range of interest is shown in Fig. 5.2 where the experimental channels were used and AWGN noises were added in the simulation. The line with square marker shows the theoretical results, which means the MMSE-IC was implemented by matrix inversion and the LLR was calculated by the exact expression with floating-point arithmetic. In the fixed-point simulation,

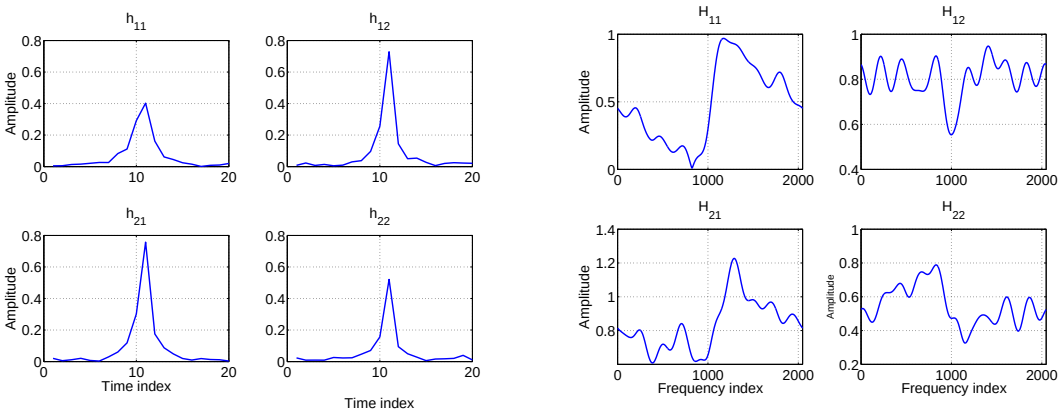

(a) The channel impulse response. (b) The frequency impulse response.

Figure 5.1. The experimental sub-channels.

the word-length was 16 bits including 13 bits for the fractional part, 2 bits for the integer part and 1 bit for the sign. MMSE-IC was implemented by QRD and back substitution and the LLR was calculated by the approximation (20) and (23). We can see that the fixed-point and floating-point systems have very similar performance. After three iterations, the detector can obtain about 1 dB gain at 10^{-3} BER over one iteration.

In the scheme of 16-matrix pipelining QRD combined with 1-D back substitution, 16 equivalent channel matrices are fed into the QRD module in 16 clock cycles at a batch. After 479 clock cycles, the 16 groups of $\mathbf{R}$ and $\mathbf{Z}_H$ matrices are output by pipelining in 16 clock cycles. When the output of the QRD is available, the 1-D back substitution module begins to solve one group of $\mathbf{R}$ and $\mathbf{Z}_H$ in 16 clock cycles; meanwhile, the next group of 16 matrices are fed into the QRD module. In the scheme of 64-matrix pipelining combined with 2-D back substitution, we solve 64 equivalent channel matrices by pipelining in 64 clock cycles, and the overall output latency is 432 clock cycles.

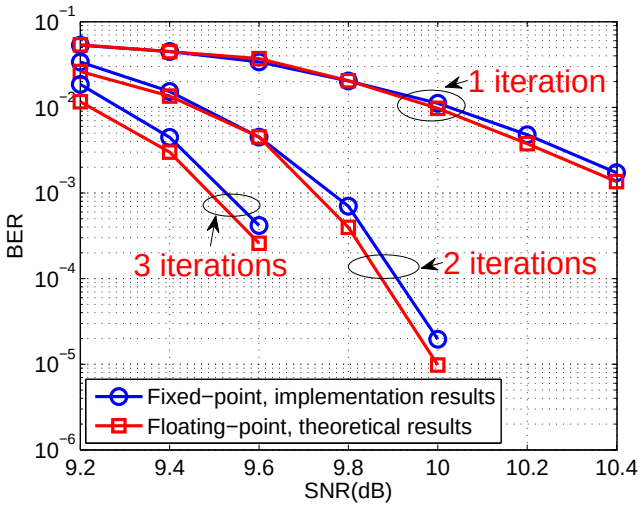

Figure 5.2. The BER performance versus SNR.

For comparison purpose, we also implemented the two systolic array QRD structures. Since the throughput of the SA-QRD-I scheme is 16 clock cycles per matrix, a 1-D array back substitution is fast enough to match the throughput of the QRD scheme. However, the SA-QRD-II scheme requires only four clock cycles to decompose one matrix, thus this architecture requires a 2-D back substitution array.

The proposed 4-CORDIC QRD and the SA-QRD architectures are synthesized on Stratix IV EP4SGX530N2 FPGA with 530K LEs, and the resource usages are shown in Table 5.1 and Table 5.2, where BS means back substitution for convenience. The calculated QRD rate is also shown in the table to compare the overall MMSE-IC throughput.

The proposed 16-matrix pipelining QRD uses the least resources still yielding a good throughput of 31 clock cycles per matrix. In the implemented MIMO-OFDM system, the channel matrices are available ahead of the received data symbols. Therefore, the QRD and back substitution are performed when the channel estimation information is available. In this case, there is enough time to perform QRD and

Table 5.1. Synthesized results of the proposed 4-CORDIC designs.

	16-matrix pipelining QRD + 1-D BS	64-matrix pipelining QRD + 2-D BS
Combinational ALUTs	6213+2302	6883+5043
DSP 18-bit Elements	48+56	168+128
DSP multiplier	24+14	84+32
QRD rate (matrix/clk)	1/31	1/7
Baseband Rx total	24%	27%
Maximal frequency	183 MHz	178 MHz

Table 5.2. Synthesized results of the conventional SA schemes.

	SA-QRD-I + 1-D BS	SA-QRD-II + 2-D BS
Combinational ALUTs	41928+2302	81639+5043
DSP 18-bit Elements	0+56	0+128
DSP multiplier	0+14	0+32
QRD rate (matrix/clk)	1/16	1/4
Baseband Rx total	33%	46%
Maximal frequency	177 MHz	170 MHz

back substitution, and we reduce the throughput for low resource usage. The 16-matrix pipelining QRD plus 1-D back substitution obtain the best tradeoff between throughput and resource usage in this system.

The proposed 64-matrix pipelining QRD plus 2-D back substitution architecture improves the throughput to seven clock cycles per matrix with slightly more resource usage than the 16-matrix pipelining scheme. Both of the proposed schemes take the advantage of the available DSP multipliers on the FPGA chip and save resources on combinational ALUTs. In comparison, the two SA-QRD schemes use no DSP elements for QRD but significantly more ALUTs to implement the Givens rotation. With only 16% of ALUTs of the SA-QRD-I scheme, the proposed 64-matrix

pipelining QRD scheme achieves more than double the throughput of the SA-QRD-I scheme. Furthermore, the SA-QRD-II uses 14 times ALUTs of the proposed 64-matrix pipelining QRD, but only achieved less than double the throughput. The latencies of the proposed two QRD schemes are 479 clock cycles and 432 clock cycles, respectively; while that of the SA-QRD-I and SA-QRD-II schemes are 480 clock cycles and 468 clock cycles, respectively. For the overall baseband receiver including digital down converters, MMSE-IC turbo detector, LDPC decoders, etc., the resource usages of the Stratix IV EP4SGX530N of the four QRD schemes are 24%, 27%, 33%, and 46%, respectively.

6 CONCLUSION

In this paper, we have implemented the iterative MIMO-OFDM receiver including MMSE-IC detector, channel estimator, LDPC decoder and other supporting modules. To solve the MMSE-IC problem, the 4-CORDIC QRD architecture and back substitution with systolic array are proposed. For an equivalent 4×4 MIMO with 1024 subcarrier OFDM, the proposed 4-CORDIC QRD can be configured as 16-matrix or 64-matrix pipelining, which are then combined with 1-D or 2-D back substitution. The channel estimator implements a frequency domain LS channel estimation with the CSD method, thanks to the character of the ZC sequence used as the pilot. In the LDPC decoder, the min-sum algorithm is implemented for QC-LDPC decoding. The two schemes for MMSE-IC detector have been implemented on FPGA for a baseband receiver, and their resource usages, throughput, and latencies are compared with classic systolic array architectures. The 16-matrix pipelining scheme uses the least resources and achieves a throughput of 31 clock cycles per matrix. The 64-matrix pipelining scheme has a high throughput of seven clock cycles per matrix with slightly increased resource usage. In contrast, the SA-QRD-I and SA-QRD-II schemes achieve 16 clock cycles and four clock cycles per matrix throughput, respectively, at a cost of much higher resource usages than the proposed schemes.

7 REFERENCES

[1] S. Haene, D. Perels, and A. Burg, "A real-time 4-stream MIMO-OFDM transceiver: System design, FPGA implementation, and characterization," *IEEE J. Sel. Areas Commun.*, vol. 26, no. 6, pp. 877–889, Aug. 2008.

[2] C. Douillard, M. Jézéquel, C. Berrou, A. Picart, P. Didier, A. Glavieux *et al.*, "Iterative correction of intersymbol interference: Turbo-equalization," *European Trans. Telecomm.*, vol. 6, no. 5, pp. 507–511, 1995.

[3] M. Tuchler, R. Koetter, and A. Singer, "Turbo equalization: principles and new results," *IEEE Trans. Commun.*, vol. 50, no. 5, pp. 754–767, May 2002.

[4] L. Boher, R. Rabineau, and M. Helard, "FPGA implementation of an iterative receiver for MIMO-OFDM systems," *IEEE J. Sel. Areas Commun.*, vol. 26, no. 6, pp. 857–866, Aug. 2008.

[5] R.-H. Chang, C.-H. Lin, K.-H. Lin, C.-L. Huang, and F.-C. Chen, "Iterative QR decomposition architecture using the modified gram-schmidt algorithm for MIMO systems," *IEEE Trans. Circuits Syst. I, Reg. Papers*, vol. 57, no. 5, pp. 1095–1102, May 2010.

[6] Z.-Y. Huang and P.-Y. Tsai, "Efficient implementation of QR decomposition for gigabit MIMO-OFDM systems," *IEEE Trans. Circuits Syst. I, Reg. Papers*, vol. 58, no. 10, pp. 2531–2542, Oct. 2011.

[7] J. E. Volder, "The CORDIC trigonometric computing technique," *IRE Trans. Electron. Comput.*, vol. EC-8, no. 3, pp. 330–334, Sep. 1959.

[8] Y. R. Zheng, M. Wang, W. Zeng, and C. Xiao., "Practical linear precoder design for finite alphabet multiple-input multiple-output orthogonal frequency division multiplexing with experiment validation," *IET Commun.*, vol. 7, no. 9, pp. 836–847, Jun. 2013.

[9] N. Jiang, K. Peng, J. Song, C. Pan, and Z. Yang, "High-throughput QC-LDPC decoders," *IEEE Trans. Broadcast.*, vol. 55, no. 2, pp. 251–259, Feb. 2009.

[10] "AN 506: QR matrix decomposition," Altera, Tech. Rep., Feb. 2008. [Online]. Available: `http://www.altera.com/literature/an/an506.pdf`

[11] K. Yao and F. Lorenzelli, "Systolic algorithms and architectures for high-throughput processing applications," *J. Signal Processing Syst.*, vol. 53, no. 1, pp. 15–34, 2008.

[12] P. Quinton, *Systolic Algorithms and Architectures.* Hemel Hempstead: Prentice Hall, 1991.

[13] G. Lightbody, R. Woods, and R. Walke, "Design of a parameterizable silicon intellectual property core for QR-based RLS filtering," *IEEE Trans. Very Large Scale Integr. (VLSI) Syst.*, vol. 11, no. 4, pp. 659 –678, Aug. 2003.

[14] D. Chu, "Polyphase codes with good periodic correlation properties," *IEEE Trans. Inform. Theory,*, vol. 18, no. 4, pp. 531–532, Jul. 1972.

[15] T. J. Richardson and R. L. Urbanke, "Efficient encoding of low-density parity-check codes," *IEEE Trans. Inform. Theory*, vol. 47, no. 2, pp. 638–656, Feb. 2001.

[16] H. Lou and C. Xiao, "Soft-decision feedback turbo equalization for multilevel modulations," *IEEE Trans. Signal Proc.*, vol. 59, no. 1, pp. 186–195, Jan. 2011.

[17] H. Kwan, "Simple sigmoid-like activation function suitable for digital hardware implementation," *Electron. lett.*, vol. 28, no. 15, pp. 1379–1380, Jul. 1992.

II. FPGA IMPLEMENTATION OF QR DECOMPOSITION FOR MIMO-OFDM USING FOUR CORDIC CORES

Bing Han, Zengli Yang and Yahong Rosa Zheng, *Senior Member, IEEE*

ABSTRACT—A low-resource implementation of QR decomposition (QRD) is proposed for MIMO-OFDM systems that employ turbo MMSE-IC (Minimum mean square error interference cancellation) detector. The proposed implementation uses only four CORDIC cores for QR decomposition of complex-valued matrices while existing systolic array architecture requires 15 to 38 CORDIC cores to achieve similar throughput. For 4-by-4 MIMO with 1024 subcarrier OFDM, the turbo MMSE-IC requires 1024 QRD of 4-by-4 complex matrices followed by back substitution. Each matrix QRD is accompanied by rotations of four vectors for the second and subsequent turbo iterations. The proposed architecture implements the multiple vector rotation by multipliers rather than CORDIC cores, thus saving resources. When combined with a 2-dimensional array of back substitution, the proposed QRD architecture can achieve 64-matrix pipelining and a throughput of seven clocks per matrix for MMSE-IC calculation. The proposed MMSE-IC architecture has been implemented in Altera Stratix IV FPGA with LDPC decoding and other baseband receiver components.

ACKNOWLEDGEMENT

This work was supported in part by the National Science Foundation under Grant ECCS-0846486. We thank Dr. Chengshan Xiao for his helpful advices during the development of the work. Part of the hardware implementation was done by Drs. Huang Lou and Mingxi Wang, who were members of the project team.

1 INTRODUCTION

Multiple-input multiple-output orthogonal frequency-division multiplexing (MIMO-OFDM) techniques has been widely used in recent wireless communication systems and standards [1, 2]. To combat Co-Channel Interference (CCI) inherent in MIMO systems, turbo iterative detector is often required to achieve high performance. Turbo MIMO detection is similar to the turbo equalizers proposed for multi-path channels to combat inter-symbol interference (ISI) [3, 4, 5]. The Minimum Mean Square Error (MMSE) turbo linear equalizer with interference cancelation (MMSE-IC) [4, 6, 7] is shown to achieve good tradeoff between computational complexity and Bit-Error-Rate (BER) performance.

A design challenge in turbo iterative detection of MIMO-OFDM is the increased computational complexity because matrix inversion is required to solve a large set of system equations. For example, for a 2×2 MIMO with 2048 subcarriers employing precoder and 2-subcarrier grouping, the turbo receiver has to perform matrix inversion for the 1024 equivalent channel matrices of size 4×4. In hardware implementation, matrix inversion is usually accomplished by QR decomposition (QRD) followed by back substitution. Commonly used QR decomposition algorithms include Gram-Schmidt, Householder transformation, and Givens rotation [8, 9]. With the CORDIC cores widely available [10], Givens rotation is adopted in many recent works with the systolic array architecture [7, 11, 9].

Most of the QRD implementation considers the system equation of the form $\mathbf{As} = \mathbf{b}$ with $\mathbf{A}$ being the matrix to be decomposed, $\mathbf{s}$ being the variable vector to be solved, and $\mathbf{b}$ being the observation vector. With MMSE-IC turbo detection, however, the Givens rotations of each channel matrix have to be applied to multiple observation vectors that are the received signal minus the reconstructed interference

from the detected symbols of the previous iteration. That is, each matrix QRD is accompanied by rotations of multiple observation vectors for the second and subsequent turbo iterations. With the same channel matrix $\mathbf{A}$, the observation vector for each symbol is different, thus giving rise to a set of system equations for each subcarrier. Additionally, back substitution is also performed for the multiple vectors. These impose more computational complexity and latency than that with no interference cancellation. The systolic array implementation will have to either increase the number of internal cells or reduce throughput to perform the MMSE-IC turbo detection.

In this paper, we implement the MMSE-IC iterative detector with a 4-CORDIC architecture for QRD and a 2-D array for back substitution. The proposed architecture implements the multiple vector rotation by multipliers rather than CORDIC cores, thus saving resources. When combined with a 2-D array of back substitution, the proposed QRD architecture can achieve good balance between resource usage and throughput. For 4×4 MIMO with 1024 subcarrier OFDM, the proposed scheme achieves 64-matrix pipelining and a throughput of seven clocks per matrix for MMSE-IC detection. In contrast, the systolic array architecture [10] has to reuse the one-vector rotation four times for MMSE-IC detection, thus reducing the pipelining to 32 matrices. Consequently, a 1-D array is fast enough for the back substitution yielding a throughput of 16 clocks per matrix. The proposed architecture uses the 6% of the resources of the Altera Stratix IV EP4SG530N FPGA less than the systolic array QRD approach.

2 TURBO MMSE DETECTION WITH INTERFERENCE CANCELATION

Consider a MIMO-OFDM system with N_t transmit antennas, N_r receive antennas, and K_c subcarriers. The signal frame structure of transmitter is shown in Fig. 2.1, where the pilot and data blocks are transmitted separately with their own cyclic prefix. The length of data blocks is determined by channel variation and we assume the channel remains unchanged in the duration of the data blocks. With linear precoding and/or subcarrier grouping [12], every K_G subcarriers are grouped together and the MIMO-OFDM channel is equivalent to K_c/K_G subcarrier with $M \times N$ MIMO, where $M = N_r \cdot K_G$ and $N = N_t \cdot K_G$.

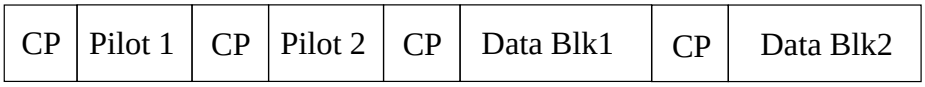

Figure 2.1. Transmitted signal frame structure, where CP = cyclic prefix.

The MMSE-IC turbo detector is shown in Fig. 2.2, where the front end processes the received signals and outputs baseband I and Q signals and remove the CPs. The pilot blocks are used for channel estimation yielding the frequency domain channel coefficients, and the data blocks are converted to frequency domain via Fast Fourier Transform (FFT). Soft symbol LLRs are exchanged between the MMSE-IC MIMO detector and the channel decoder for turbo detection.

Let $\mathbf{y}_k \in \mathbb{C}^{M\times 1}$ and $\mathbf{H}_{e,k} \in \mathbb{C}^{M\times N}$ denote the received vector and the equivalent channel matrix of the k-th sub-channel, respectively. We have

$$\mathbf{y}_k = \mathbf{H}_{e,k}\mathbf{s}_k + \mathbf{v}_k, \qquad k = 1, 2, ..., K_c/K_G \tag{1}$$

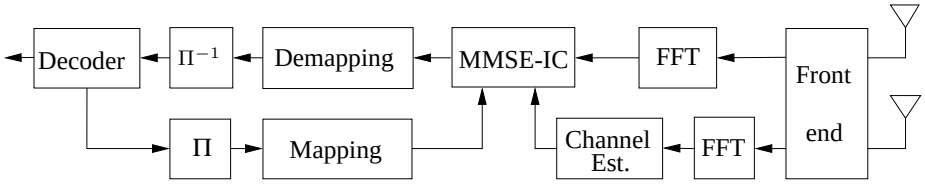

Figure 2.2. The block diagram of turbo MMSE-IC receiver, where Π is the interleaver and Π^{-1} is the de-interleaver.

where $\mathbf{s}_k \in \mathbb{C}^{N\times 1}$ is the transmitted symbol vector and $\mathbf{v}_k \in \mathbb{C}^{M\times 1}$ is the noise vector with power σ_v^2. In the first iteration, no prior LLR is available, thus the MMSE-IC computes the estimate of the symbol vector by

$$\hat{\mathbf{s}}_k = (\mathbf{H}_{e,k}^H \mathbf{H}_{e,k} + \sigma_v^2 \mathbf{I})^{-1} \mathbf{H}_{e,k}^H \mathbf{y}_k, \tag{2}$$

where superscript ^{H} denotes the Hermitian transpose. Solving (2) is usually accomplished by solving the linear system equation [7] as

$$\mathbf{A}\mathbf{s} = \mathbf{b} \tag{3}$$

where $\mathbf{A} = \mathbf{H}_{e,k}^H \mathbf{H}_{e,k} + \sigma_v^2 \mathbf{I}$ and $\mathbf{b} = \mathbf{H}_{e,k}^H \mathbf{y}_k$.

In the second and subsequent iterations, the MMSE-IC detector reconstructs the interference by

$$\mathbf{y}'_{k,n} = \mathbf{y}_k - \mathbf{H}_{e,k} \tilde{\mathbf{s}}_{k,n}, \tag{4}$$

where $\tilde{\mathbf{s}}_{k,n} = [\hat{s}_{k,1}, ..., \hat{s}_{k,n-1}, 0, \hat{s}_{k,n+1}, ..., \hat{s}_{k,N}]$ with $\hat{s}_{k,n}$ being the estimated symbols from the previous iteration. Then the MMSE-IC detector computes the n-th symbol of the k-th subcarrier by

$$\hat{s}_{k,n} = \mathbf{e}_n (\mathbf{H}_{e,k}^H \mathbf{H}_{e,k} + \sigma_v^2 \mathbf{I})^{-1} \mathbf{H}_{e,k}^H \mathbf{y}'_{k,n}, \quad n = 1, 2, ..., N. \tag{5}$$

where $\mathbf{e}_n$ is a $1 \times N$ vector with all elements equal to 0 except the n-th element that is equal to 1.

Equation (5) can also be viewed as the solution to a set of linear system equations:

$$\mathbf{AX} = \mathbf{B} \tag{6}$$

where $\mathbf{X} = \text{diag}(\mathbf{s}_k)$, and the n-th column of $\mathbf{B}$ is $\mathbf{H}_{e,k}^{H}\mathbf{y}'_{k,n}$.

3 ARCHITECTURE OF QRD AND BACK SUBSTITUTION

It is well known that QRD and BS are used to solve the linear system equations (3) and (6). Let $\mathbf{A} = \mathbf{QR}$ denote the QR decomposition. Traditionally, the Givens rotation method rotates the elements of $\mathbf{A}$ and $\mathbf{b}$ to yield $\mathbf{R}$ and $\mathbf{z} = \mathbf{Q}^H\mathbf{b}$ without explicitly solving for $\mathbf{Q}$. This is often implemented by a systolic array architecture [7, 9] using CORDIC cores to find rotation angles. Then back substitution solves (3) for $\mathbf{s}$ by computing

$$s_n = \frac{1}{r_{nn}} \left(z_n - \sum_{j=n+1}^{N} r_{nj} s_j \right), \quad n = N, ..., 2, 1, \tag{7}$$

where s_n is the n-th element of $\mathbf{s}$ and r_{nj} is the (n, j)-th element of $\mathbf{R}$. Back substitution is often implemented by a 1-D array [8].

To solve (6) for the diagonal elements of $\mathbf{X}$, the multiple column vectors in $\mathbf{B}$ can be rotated by the systolic array in two ways: One is to rotate all columns of $\mathbf{B}$ simultaneously by adding more internal elements in the systolic array; another is to rotate one column at a time by reusing the same architecture of the single column system as that for (3).

3.1 THE PROPOSED 4-CORDIC QRD AND 2-D BACK SUBSTITUTION

In this subsection, we propose an alternative approach to QR decomposition without using systolic array. We use only four CORDIC cores and some complex-valued multipliers to implement the Givens rotation directly. This is motivated by two observations related with the MMSE-IC turbo detection. First, for the signal frame structure shown in Fig. 2.1, the channel matrices of all subcarriers are available way ahead of the received data symbols and remain unchanged within the data frame.

Therefore, the QR decomposition can be performed before the arrival of the data signals and be saved for later use with all data blocks. This approach relaxes the throughput and timing requirements of the QRD. To illustrate approach, we focus on solving the system equations (6) since (3) is a special case of (6). To separate the channel matrix from the data vectors, we modify the matrix $\mathbf{B}$ as

$$\mathbf{B} = \mathbf{H}_{e,k}^{H}, \tag{8}$$

and compute the QRD of $\mathbf{A}$ to yield the $\mathbf{R}$ matrix and $\mathbf{Z} = \mathbf{Q}^{H}\mathbf{B}$. When a data block is available, we only multiply the solution $\mathbf{Z}$ with $\mathbf{y}'_{k,n}$ to obtain the estimated symbols.

The second observation on the MMSE-IC detector is that matrix $\mathbf{A}$ is positive semi-definite and its diagonal elements are all real. If a_{ii} is used to zero the elements a_{ji} with $j > i$, then a_{ii} remains real through the i-th column zeroing. This observation helps to save two CORDIC cores in our proposed QRD architecture. The block diagram of the proposed QRD is shown in Fig. 3.1, where the first rotation is depicted as an example. The first input to the QRD module (denoted as qr_sub) is always the diagonal element of $\mathbf{A}$ and it is always real. Therefore, its sign and amplitude are easily obtained via the absolute value module ABS. The second input to qr_sub is a complex element a_{21}, and CORDIC 1, operating in the vectoring mode, computes the amplitude $|a_{21}|$ and phase φ. The amplitudes $|a_{11}|$ and $|a_{21}|$ are fed to CORDIC 2. Also set in the vectoring mode, CORDIC 2 outputs the phase $\theta = \tan^{-1}(|a_{21}|/|a_{11}|)$ and the amplitude $a_{11}^{(1)} = \sqrt{|a_{11}|^2 + |a_{21}|^2}$, which is used for the next rotation. CORDIC 3 takes the input θ and operates in the rotation mode to yield $\cos(\theta)$ and $\sin(\theta)$. The SEL block takes the sign of a_{11} and flips the sign of $\cos(\theta)$ if $\text{sign}(a_{11}) < 0$, which outputs the rotation coefficient $C_{(1)} = \text{sign}(a_{11})\cos(\theta)$.

The NEG block changes the sign of φ and outputs to CORDIC 4. Operating in the rotation mode, CORDIC 4 computes $S_{(1)} = \sin(\theta)e^{-j\varphi}$.

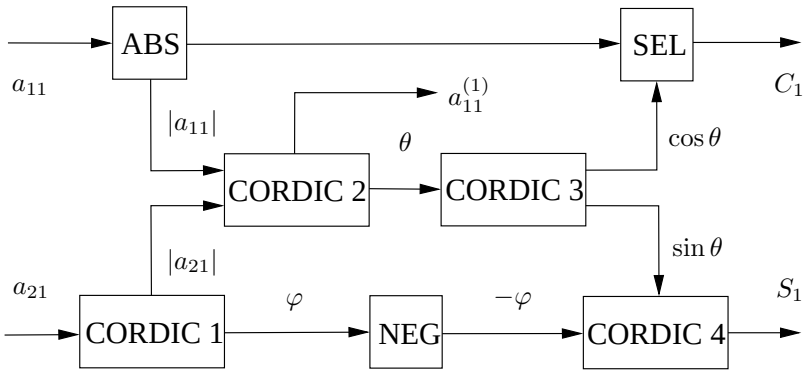

Figure 3.1. The block diagram of qr_sub module.

The coefficients C_1 and S_1 are used to form a Givens rotation matrix. To illustrate our architecture, we consider a 4×4 complex matrix $\mathbf{A}$ as an example. The Givens rotation matrix for zeroing a_{21} is

$$\mathbf{G}_1 = \begin{bmatrix} C_1 & S_1 & 0 & 0 \\ -S_1^H & C_1^H & 0 & 0 \\ 0 & 0 & 1 & 0 \\ 0 & 0 & 0 & 1 \end{bmatrix} \tag{9}$$

and $\mathbf{G}_1$ is used to rotate the remaining elements in row 1 and 2 of $\mathbf{A}$. In our hardware implementation, we use three qr_mul modules to accomplish this task:

$$\begin{aligned} a_{1j}^{(1)} &= C_1 a_{1j} + S_1 a_{2j} \\ a_{2j}^{(1)} &= -S_1^H a_{1j} + C_1^H a_{2j} \end{aligned} \tag{10}$$

where $j = 2, 3, 4$, and the superscript represents the count of rotations. Each qr_mul module uses 12 real 18-bit multipliers.

Similarly, rotation of the first two rows of matrix **B** is performed with four qr_mul modules. After the first rotation, the QRD inputs are changed to $a_{11}^{(1)}$ and a_{31} for the second rotation to yield the rotation coefficients C_2 and S_2, followed by multiplications to yield $a_{1j}^{(2)}$ and $a_{3j}^{(2)}$ for $j = 2, 3, 4$. In total, six rounds of rotations are required to complete the QRD of a 4×4 matrix.

Due to the latency of the CORDIC cores, the 4-CORDIC architecture exhibits 83 clocks of delay. Pipelining of 64 matrices is utilized in our implementation to boost the throughput. The timing control of the qr_sub and qr_mul modules is shown in Fig. 3.2, where qr_mul 2, 3, and 4 are used for parallel rotation of columns 2–4 of matrix **A**. The timing gap before the input of $a_{33}^{(4)}, a_{43}^{(5)}$ is due to the latency of $a_{43}^{(5)}$ that is the output of qr_mul 3. Meanwhile, the rotation of matrix **B** is performed by another four qr_mul modules since matrix **B** always has four elements in each row for rotation. The timing of the four qr_mul to rotate matrix **B** is the same as the qr_mul 4 and is omitted from the figure for brevity.

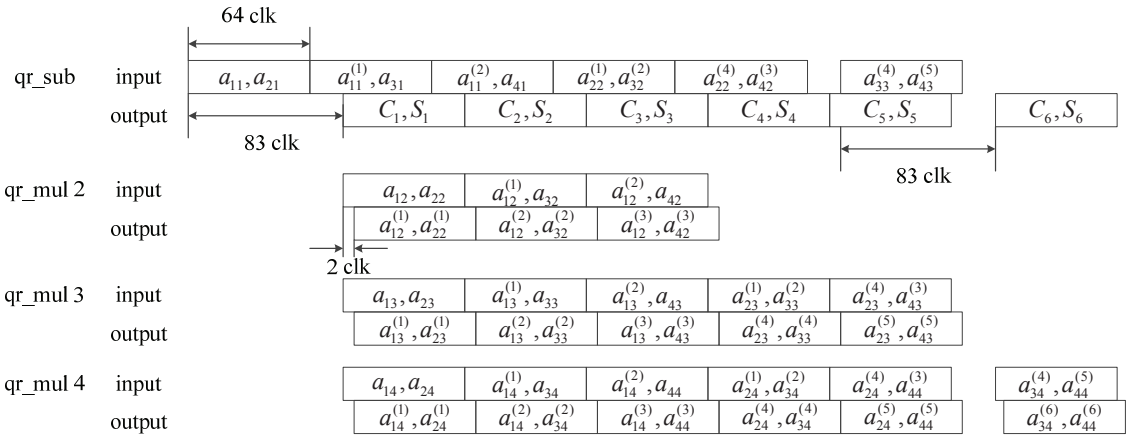

Figure 3.2. Timing control for 4-CORDIC QRD.

The 64-matrix pipelining yields a high throughput of seven clocks per matrix. Consequently, we use a 2-D systolic array for back substitution, as shown in Fig. 3.3. The red numbers denote the input and output timing in clock count. The throughput of the 2-D back substitution is one clock per vector of **Z**, resulting in four clocks total for solving (6). The latency is seven clocks.

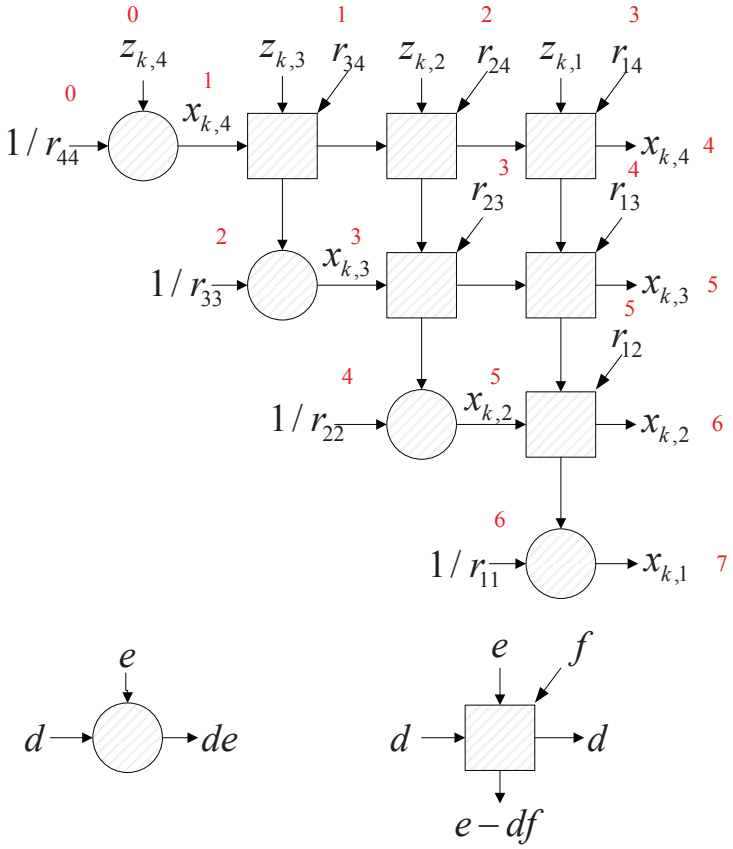

Figure 3.3. 2-D systolic arrays for back substitution.

3.2 THE SYSTOLIC ARRAY QRD AND 1-D BACK SUBSTITUTION

For comparison purpose we also implement the QRD with the systolic array (SA-QRD) [10] that uses four boundary cells and ten internal cells which is shown in

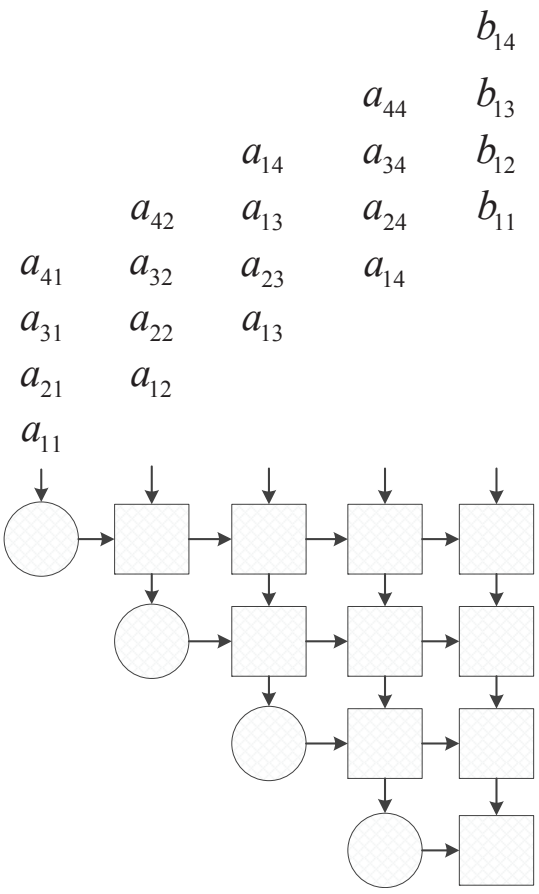

Figure 3.4. Conventional systolic array QRD for solving $\mathbf{As} = \mathbf{b}$.

Fig. 3.4. The total number of CORDIC cores is 38 since each boundary cell uses two CORDIC cores for complex vector mode, and each internal cell uses three CORDIC cores for complex rotation mode. With only one column for rotating the elements of matrix **B**, we reuse the QRD four times to rotate the four columns **B**. Since the QRD latency of the systolic array is 80 clocks, the throughput of the 2-D systolic array QRD is 16 clocks per matrix. Therefore, a 1-D array back substitution is fast enough to match the speed of the QRD [8]. The overall throughput is 16 clocks per matrix operation of MMSE-IC, while the resource usage is 38 CORDIC cores with 14 real multipliers.

4 SIMULATION AND SYNTHESIS RESULTS

To examine the performance of the proposed QRD and BS, a 2×2 MIMO 2048-subcarrier OFDM system is built [12] with 2-subcarrier grouping. The data blocks at the transmitter are generated by two raw source bit streams encoded by a length-2040 LDPC encoder with 3/4 coding rate. After LDPC encoding, each codeword is added 8 bits of zeros at the end to form a data block of length 2048, which is then interleaved and modulated to QPSK or 8PSK symbols. After precoding, the symbols of each stream are fed into a subcarrier grouper. Then, each data block is converted to time domain signals by 2048-point inverse fast Fourier transform (IFFT), followed by CP insertion and pilot block insertion. The digital up convertor (DUC) is used to up-sample the baseband I/Q signals and modulate them onto IF (intermediate frequency). The output of the DUC module is fed to the digital to analog converter (DAC) directly and a RF up convertor is used to transmit the signal at 915 MHz.

The receiver with these two QRD architectures to solve MMSE-IC problem has been implemented, respectively, with digital down convertor, channel estimator, and LDPC soft decoders. Fig. 4.1 shows the simulation result of 4-CORDIC QRD and 1-D BS, where 64 equivalent channel matrices are fed into the QRD module in 64 clocks at a batch. After 432 clocks, the 64 groups of $\mathbf{R}$ and $\mathbf{Z}$ matrices are output by pipelining in 64 clocks. When the output of the QRD is available, the 2-D BS module begins to solve one group of $\mathbf{R}$ and $\mathbf{Z}$ in 4 clocks; meanwhile, the next group of 64 matrices are fed into the QRD module.

The proposed 4-CORDIC QRD and the SA-QRD architectures are synthesized on Stratix IV EP4SGX530N2 FPGA with 530K LEs. The results of resource usage are shown in Table 4.1. The calculated QRD rate is also shown in the table to compare the overall MMSE-IC throughput.

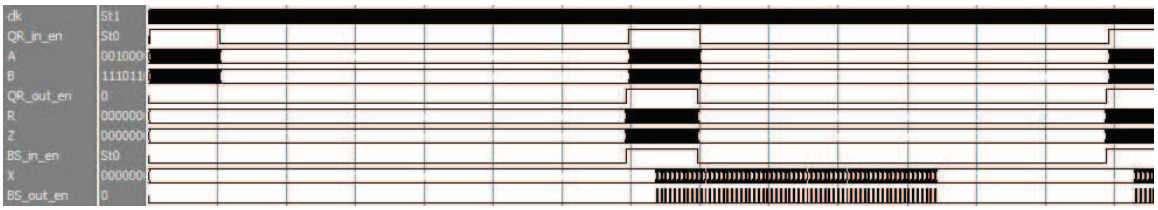

Figure 4.1. Simulation results of 4-CORDIC QRD and 2-D BS.

Table 4.1. Comparison of the conventional work and the proposed designs

	4-CORDIC QRD +2-D BS	SA QRD +1-D BS
Combinational ALUTs	6883+5043	41928+2302
DSP 18-bit Elements	168+128	0+128
DSP multiplier	84+32	0+14
QRD rate (matrix/clk)	1/7	1/16

The number of ALUTs used by the proposed 4-CORDIC architecture is about 1/7 that of the SA-QRD, but its the twice throughput. The proposed architecture uses a total of 116 real multipliers and some DSP elements that are inherent in the FPGA. The total logic utilization of baseband modules, including digital down converter, QRD, LDPC decoder, etc., is 27% when the proposed 4-CORDIC QRD is used for MMSE-IC turbo detection. In comparison, if SA-QRD and 1D BS were used for MMSE-IC turbo detection, the baseband receiver uses a total of 33% resource. The proposed architecture saves 6% of the resources of Stratix IV but achieves more than twice the throughput in comparison to the SA-QRD approach.

5 CONCLUSION

In this paper, we have implemented the MMSE-IC iterative detector with a 4-CORDIC QRD and a 2-D BS. The proposed architecture uses multipliers rather than CORDIC cores to implement the rotation of multiple vectors required in MMSE-IC turbo detection, thus saving resources and boost throughput. For 4×4 MIMO with 1024 subcarrier OFDM, the proposed scheme achieves 64-matrix pipelining and a throughput of seven clocks per matrix for MMSE-IC calculation. In comparison, the systolic array architecture that reuses the one-vector rotation four times for MMSE-IC detection only obtains a throughput of 16 clocks per matrix. The compilation results show that the proposed architecture saves 6% of the resources while achieving higher throughput than the SA-QRD approach.

6 REFERENCES

[1] A. Ghosh, D. Wolter, J. Andrews, and R. Chen, "Broadband wireless access with WiMax/802.16: current performance benchmarks and future potential," *IEEE Commun. Mag.*, vol. 43, no. 2, pp. 129 –136, feb. 2005.

[2] B. Le Floch, M. Alard, and C. Berrou, "Coded orthogonal frequency division multiplex [TV broadcasting]," *Proc. IEEE*, vol. 83, no. 6, pp. 982 –996, Jun. 1995.

[3] C. Douillard, M. Jézéquel, C. Berrou, A. Picart, P. Didier, A. Glavieux *et al.*, "Iterative correction of intersymbol interference: Turbo-equalization," *European Trans. Telecomm.*, vol. 6, no. 5, pp. 507–511, 1995.

[4] M. Tuchler, R. Koetter, and A. Singer, "Turbo equalization: principles and new results," *IEEE Trans. Commun.*, vol. 50, no. 5, pp. 754 –767, may 2002.

[5] R. Koetter, A. Singer, and M. Tuchler, "Turbo equalization," *IEEE Signal Processing Mag.*, vol. 21, no. 1, pp. 67 – 80, jan. 2004.

[6] L. Boher, R. Rabineau, and M. Helard, "An efficient MMSE equalizer implementation for 4x4 MIMO-OFDM systems in frequency selective fast varying channels," in *IEEE Int. Symp. Personal, Indoor Mobile Radio Commun. (PIMRC 2007)*, 2007, pp. 1–5.

[7] ——, "FPGA implementation of an iterative receiver for MIMO-OFDM systems," *IEEE J. Sel. Areas Commun.*, vol. 26, no. 6, pp. 857 –866, Aug. 2008.

[8] P. Quinton, *Systolic Algorithms and Architectures*. Hemel Hempstead: Prentice Hall, 1991.

[9] Z.-Y. Huang and P.-Y. Tsai, "Efficient implementation of QR decomposition for gigabit MIMO-OFDM systems," *IEEE Trans. Circuits Syst. I, Reg. Papers*, vol. 58, no. 10, pp. 2531 –2542, Oct. 2011.

[10] "AN 506: QR matrix decomposition," Altera, Tech. Rep., Feb. 2008. [Online]. Available: `http://www.altera.com/literature/an/an506.pdf`

[11] A. Maltsev, V. Pestretsov, R. Maslennikov, and A. Khoryaev, "Triangular systolic array with reduced latency for qr-decomposition of complex matrices," in *IEEE Int. Symp. Circuits Syst. (ISCAS 2006)*, May 2006, pp. 385–388.

[12] M. Wang, Y. R. Zheng, and C. Xiao, "A low complexity algorithm for linear precoder design with finite alphabet inputs," in *IEEE MilCom 2012*, Nov. 2012, pp. 1–6.

III. HIGHER-RANK PRINCIPLE KRONECKER MODEL FOR TRIPLY SELECTIVE FADING CHANNELS WITH EXPERIMENTAL VALIDATION

Bing Han and Yahong Rosa Zheng, *Senior Member, IEEE*

ABSTRACT—This paper proposes a higher-rank principle Kronecker model (PKM) for simulating triply-selective fading channels. To construct the PKM, the channel correlation matrices are decomposed using the higher-order singular value decomposition (HOSVD) method. The proposed PKM-HOSVD model improves upon the original Kronecker model by using higher-rank approximation of the channel correlation matrices rather than the rank-1 approximation. The proposed PKM-HOSVD model was validated by extensive field experiments conducted for 4-by-4 multiple-input multiple-output (MIMO) systems in both indoor and outdoor environments. The carrier frequencies used included 800 MHz, 2.2 GHz, and 5.2 GHz. The channel correlation matrices calculated from the measured channel coefficients were then decomposed via the proposed PKM-HOSVD method. The quality of the decomposition was evaluated by not only the mean square error (MSE) but also the correlation matrix distance (CMD). These results indicate that many practical channels must use higher-rank approximation rather than the commonly-used rank-1 approximation (or the Kermoal method) to achieve satisfactory decomposition accuracy. In addition, the predicted channel capacity by the proposed channel simulation model achieves better accuracy than the original rank-1 channel simulation model.

ACKNOWLEDGMENTS

The authors would like to acknowledge the funding support from Office of Naval Research under DURIP N00014-12-1-0022 and N00014-09-1-0011 projects. We acknowledge Zengli Yang for his help with setting up NI soft panel instruments. We also thank Drs. Peng Han and Xinhu Liu, visiting scholars at Missouri University of Science and Technology, for their help on the outdoor experiments.

1 INTRODUCTION

Fading channel correlation plays an important role in channel modeling and simulation [1, 2, 3, 4, 5, 6, 7], capacity analysis [8, 9], transceiver design [10, 11, 12], and performance analysis [13, 14, 15]. Assume a multiple-input multiple-output (MIMO) system with N transmit antennas and M receive antennas. For a baseband equivalent MIMO fading channel, if the fading channel length is $L > 1$ and the coherence time is $K > 1$, then such a fading channel is often characterized as a triply-selective fading channel [3], which means that the subchannels of a MIMO system are space-selective, time-selective and frequency selective. Often the correlation matrix, whose size is $(MNLK) \times (MNLK)$, can be separated into the Kronecker product of spatial, temporal, and Doppler correlation matrices of sizes $M \times M$, $N \times N$, $L \times L$, and $K \times K$, respectively. This separable channel model is referred to as the Kronecker model which is extensively validated by field measurements [16, 17, 18, 4, 19, 20, 5, 21, 7, 6, 22] and commonly adopted to model both base-to-mobile and mobile-to-mobile fading channels. Note that base-to-mobile channels are modeled by one-ring scattering model because base stations are usually elevated in height; while mobile-to-mobile channels are modeled by double-ring scattering model [23] because both the transmit and receive platforms may be surrounded by obstacles.

However, a number of field measurements and simulation analyses have found that the separable Kronecker model is often inaccurate when estimating channel capacity [24, 25], channel covariance [26, 27], and channel modeling [28]. In essence, the Kronecker model is a rank-1 approximation of the true correlation matrix through singular value decomposition. To mitigate the deficiency of the Kronecker model, two different models are introduced for decomposing spatial correlation matrices of

narrow-band fading channels: the principal Kronecker model (PKM) [26] decomposes the spatial correlation matrix with a higher-rank approximation of Kronecker products, and the tensor model [26, 27] models the narrow-band channel with the fourth-order tensor.

In this paper, we propose a higher-rank PKM for simulating triply-selective fading channels. To construct the PKM, the channel correlation matrices are decomposed using the higher-order singular value decomposition (HOSVD) [29, 30, 31] method. The proposed PKM-HOSVD model improves upon the original Kronecker model by using higher-rank approximation of the channel correlation matrices rather than the rank-1 approximation. The proposed PKM-HOSVD is validated by an experimental channel-sounding campaign based on 4×4 MIMO wideband fading channels measured in both indoor and outdoor environments with carrier frequencies of 800 MHz, 2.2 GHz, and 5.2 GHz. We adopt both the correlation matrix distance (CMD) metric [32] and mean square error (MSE) to evaluate the decomposition's accuracy. Our results confirm that many practical channels must use higher-rank approximation rather than the commonly-used rank-1 approximation (or the Kermoal method) to achieve satisfactory decomposition accuracy. In addition, the proposed simulation model can predict the channel capacity more accurately than does the original rank-1 Kronecker model. We also verify that the capacity prediction's accuracy from the Kronecker model is tied strongly to the CMD of the decomposed correlation matrices.

Notation: Italics denote scalars; boldface letters denote vectors and matrices; curlicue letters denote tensors. The estimation of matrix $\mathbf{A}$ from the measurement is denoted as $\hat{\mathbf{A}}$. The (i,j)th sub-matrix of $\mathbf{A}$ is denoted as $\mathbf{A}^{(i,j)}$; the (i,j)-th element of $\mathbf{A}$ is denoted as $\{\mathbf{A}\}_{ij}$. The transpose, Hermitian transpose, and Frobenius norm of $\mathbf{A}$ are denoted as $\mathbf{A}^T$, $\mathbf{A}^\dagger$, and $\|\mathbf{A}\|_F$, respectively. The conjugate of scalar A is A^*. The operator $tr\{\cdot\}$ denotes the trace operation; operator $\otimes$ denotes a Kronecker product; operator $vec(\cdot)$ concatenates a matrix column-wise into a vector; operator $\circ$ denotes

an outer product; operator $\times_a$ denotes an a-mode product [30]. The expectation of random variable X is denoted by $E\{X\}$.

2 THE PROPOSED HIGHER-RANK PKM FOR MIMO FADING CHANNEL

We consider a wideband MIMO wireless channel consisting of N transmit antennas and M receive antennas. The input-output relationship of the MIMO channel in the baseband discrete-time domain is

$$\mathbf{y}(k) = \sum_{l=0}^{L-1} \mathbf{h}(k,l) \cdot \mathbf{x}(k-l) + \mathbf{w}(k), \tag{1}$$

where $\mathbf{x}(k) = [x_1(k), ..., x_N(k)]^T$, $\mathbf{w}(k) = [w_1(k), ..., w_M(k)]^T$, and $\mathbf{y}(k) = [y_1(k), ..., y_M(k)]^T$ are the input vector, noise vector, and output vector at time instant k, respectively; L is the multi-path channel length; $\mathbf{h}(k,l)$ is the l-th channel taps at time instant k whose (m,n)-th element $h_{m,n}(k,l)$ denotes the sub-channel linking the n-th transmit antenna to the m-th receive antenna. The dimensions of $\mathbf{x}(k)$, $\mathbf{y}(k)$, $\mathbf{w}(k)$ and $\mathbf{h}(k,l)$ are $N \times 1$, $M \times 1$, $M \times 1$ and $M \times N$, respectively.

Denote the channel coefficients measured at time instant k as $\mathbf{h}_{m,n}(k) = [h_{m,n}(k,0), \cdots, h_{m,n}(k,l),$
$\cdots, h_{m,n}(k,L-1)]^T$. The concatenated channel vector at time k is then

$$\mathbf{h}_v(k) = \left[\mathbf{h}_{1,1}^T(k), \cdots, \mathbf{h}_{M,1}^T(k), \cdots, \mathbf{h}_{1,N}^T(k), \cdots, \mathbf{h}_{M,N}^T(k)\right]^T. \tag{2}$$

The $(MNL) \times (MNL)$ dimensional channel correlation matrix is then computed as

$$\mathbf{R}(\Delta k) = E_k\{\mathbf{h}_v(k) \cdot \boldsymbol{h}_v^\dagger(k+\Delta k)\}. \tag{3}$$

The expectation $E_k[\cdot]$ is performed with respect to k because the MIMO channel is assumed to be ergodic.

In many cases, the correlation matrix $\mathbf{R}$ of a triply-selective fading channel can be decomposed into a Kronecker product of correlation matrices [3] such that

$$\mathbf{R}(\Delta k) = \mathbf{\Psi}_{tx} \otimes \mathbf{\Psi}_{rx} \otimes \mathbf{\Psi}_{tap} \cdot \Psi_{Dpl}(\Delta k), \tag{4}$$

where $\mathbf{\Psi}_{tx} \in \mathbb{C}^{N\times N}$, $\mathbf{\Psi}_{rx} \in \mathbb{C}^{M\times M}$, and $\mathbf{\Psi}_{tap} \in \mathbb{C}^{L\times L}$ are the transmit, receive, and intertap correlation matrices, respectively; $\Psi_{Dpl}(\Delta k)$ is the correlation coefficient due to the Doppler spread. In the base-to-mobile channel, $\Psi_{Dpl}(\Delta k)$ is given by [3]

$$\Psi_{Dpl}(\Delta k) = J_0(2\pi f_d \Delta k T_s), \tag{5}$$

where T_s is the symbol duration, f_d is the maximum Doppler frequency, and $J_0(\cdot)$ is the zero-order Bessel function of the first kind. In the mobile-to-mobile channel, Ψ_{Dpl} is given by [33]

$$\Psi_{Dpl}(\Delta k) = \prod_{i=1}^{2} \frac{I_0(\sqrt{\kappa_i^2 - 4\pi^2 f_{d_i}^2 \Delta k^2 + j4\pi\kappa_i f_{d_i} \Delta k \cos\mu_i})}{I_0(\kappa_i)}, \tag{6}$$

where $I_0(\cdot)$ is the zero-order modified Bessel function of the first kind, μ_i is the mean direction of either the angle of arrival (AoA) or angle of departure (AoD), and κ_i is the concentration parameter that controls the width of the scatterers on a ring. The index $i = 1, 2$ indicates the rings around the transmitter and receiver, respectively. In this model, the scatters around the transmitter and the receiver are modeled by two independent rings. The von Mises probability density function is adopted for the angle of departure surrounding the transmitter and the angle of arrival surrounding the receiver.

In the measurement, we set $\Delta k = 0$ and focused on the Kronecker decomposition of transmit, receive, and intertap correlation matrices. The observing window selected was small so that the effect of the Doppler spread can be ignored. As a result,

the decomposition of the correlation matrices was denoted as

$$\mathbf{R}_{WB} = \mathbf{\Psi}_{tx} \otimes \mathbf{\Psi}_{rx} \otimes \mathbf{\Psi}_{tap}. \tag{7}$$

As a special case, the narrow-band channel impulse response (CIR) has only one tap. Therefore, $L = 1$ and $\mathbf{\Psi}_{tap}$ is reduced to a fading gain. The Kronecker model in (7) is then simplified as [2, 34]

$$\mathbf{R}_{NB} = \mathbf{\Psi}_{tx} \otimes \mathbf{\Psi}_{rx}. \tag{8}$$

where the dimension of $\mathbf{R}_{NB}$ is $(MN) \times (MN)$.

A popular MIMO channel simulation model that divides the MIMO correlation matrices into separate receive and transmit correlation matrices is given by [2, 34]

$$\mathbf{h} = \mathbf{\Psi}_{rx}^{1/2} \mathbf{G} \mathbf{\Psi}_{tx}^{1/2}, \tag{9}$$

where $\mathbf{A}^{1/2}$ is the matrix square root defined by $\mathbf{A} = \mathbf{A}^{1/2} \cdot (\mathbf{A}^{1/2})^{\dagger}$, which can be calculated through several different methods shown in [35]; $\mathbf{G}$ is an $M \times N$ matrix whose entries are independent and identically distributed (i.i.d.) zero-mean complex-normal random Gaussian variables. No Doppler effect is considered in (9).

In contrast, Xiao [3] provided the channel simulation model for triply selective MIMO Rayleigh fading channels that considered both Doppler effects and all correlation matrices:

$$\mathbf{h}_v(k) = (\mathbf{\Psi}_{tx}^{1/2} \otimes \mathbf{\Psi}_{rx}^{1/2} \otimes \mathbf{\Psi}_{tap}^{1/2}) \cdot \mathbf{\Phi}(k), \tag{10}$$

where $\mathbf{\Phi}(k)$ is an $(MNL) \times 1$ vector whose elements are uncorrelated Rayleigh flat fading, and

$$E\{\mathbf{\Phi}(k_1) \cdot \mathbf{\Phi}^{\dagger}(k_2)\} = \Psi_{Dpl}(\Delta k). \tag{11}$$

where $\Delta k = k_1 - k_2$.

In practical scenarios, however, the channel simulation model that is based on the rank-1 Kronecker model always underestimates the channel capacity [25, 24]. Therefore, we propose the principal Kronecker model for wideband channels using higher-rank approximations as

$$\mathbf{R}_{WB} = \sum_{i=1}^{M_k} \mathbf{\Psi}_{tx,i} \otimes \mathbf{\Psi}_{rx,i} \otimes \mathbf{\Psi}_{tap,i}. \tag{12}$$

where M_k is a user-defined parameter that depends on the required accuracy. Both (7) and (8) are rank-1 approximations of the principal Kronecker model. Larger M_k will lead to better accuracy but it will increase computational complexity too. We will find the best trade-off between accuracy and complexity by using a metric as the threshold for choosing M_k in Section 5.2.

The channel simulation model for triply selective Rayleigh fading channels is improved according to (10) and (12) as

$$\mathbf{h}_v(k) = \sum_{i=1}^{M_k} [(\mathbf{\Psi}_{tx,i}^{1/2} \otimes \mathbf{\Psi}_{rx,i}^{1/2} \otimes \mathbf{\Psi}_{tap,i}^{1/2}) \cdot \mathbf{\Phi}(k)]. \tag{13}$$

The Kermoal decomposition method in [1, 27] estimates both the transmit and the receive correlation matrices of the narrow-band channel, and can be applied

directly to the wideband channel to obtain the rank-1 Kronecker model:

$$\begin{aligned} \hat{\mathbf{\Psi}}_{tx} &= E_{k,l}\{[\mathbf{h}^{\dagger}(k,l)\mathbf{h}(k,l)]^{T}\}, \\ \hat{\mathbf{\Psi}}_{rx} &= E_{k,l}\{\mathbf{h}(k,l)\mathbf{h}^{\dagger}(k,l)\}, \\ \hat{\mathbf{\Psi}}_{tap} &= E_{k,m,n}\{\mathbf{h}_{m,n}(k)\mathbf{h}_{m,n}^{\dagger}(k)\}. \end{aligned} \tag{14}$$

Note that $\hat{\mathbf{\Psi}}_{tx}$ and $\hat{\mathbf{\Psi}}_{rx}$ are calculated by averaging over k and l; $\hat{\mathbf{\Psi}}_{tap}$ is calculated by averaging over k, m, and n. The narrow-band decomposition is obtained by setting $L = 1$. The Kermoal method cannot decompose the principle Kronecker model.

3 PKM DECOMPOSITION OF PRINCIPLE KRONECKER MODEL

The principle Kronecker model cannot be obtained by the Kermoal method and higher-rank decomposition required in (12) has to use HOSVD. Decomposing wideband correlation matrix $\mathbf{R}_{WB}$ into the Kronecker product of $\hat{\mathbf{\Psi}}_{tx}$, $\hat{\mathbf{\Psi}}_{rx}$ and $\hat{\mathbf{\Psi}}_{tap}$ is based on minimizing the cost function

$$\phi_{WB} = \left\| \mathbf{R}_{WB} - \sum_{i=1}^{M_k} \hat{\mathbf{\Psi}}_{tx,i} \otimes \hat{\mathbf{\Psi}}_{rx,i} \otimes \hat{\mathbf{\Psi}}_{tap,i} \right\|_F^2 . \tag{15}$$

To solve the problem in (15), we first partition $\mathbf{R}_{WB}$ into sub-matrices and construct the third-order tensor based on the sub-matrices. Then we use HOSVD to obtain the optimal estimation of $\hat{\mathbf{\Psi}}_{tx}$, $\hat{\mathbf{\Psi}}_{rx}$ and $\hat{\mathbf{\Psi}}_{tap}$. The details are listed as follows.

Step 1: $\mathbf{R}_{WB}$ is partitioned into $(MN) \times (MN)$ sub-matrices of size $L \times L$. The (m, n)-th partition is denoted as

$$\mathbf{R}_{WB}^{(m,n)} = E_k \left[\mathbf{h}_{m_1,n_1}(k) \circ \mathbf{h}_{m_2,n_2}(k) \right], \tag{16}$$

where $m_1, m_2 = 1, \cdots, M$, $n_1, n_2 = 1, \cdots, N$, and the indices (m, n) are determined by $m = m_1 + M \cdot (n_1 - 1), n = m_2 + N \cdot (n_2 - 1)$. Therefore, the correlation matrix $\mathbf{R}_{WB}$ can be re-arranged into a third-order tensor whose mode-3 is

$$\tilde{\mathcal{R}}(m, n, 1 : L^2) = vec(\mathbf{R}_{WB}^{(m,n)}). \tag{17}$$

The indices of the first two modes (m, n) of $\tilde{\mathcal{R}}$ is rearranged into

$$m' = n_1 + (q - 1)M, \quad n' = m_1 + (p - 1)N, \tag{18}$$

where $q = ceil(n/N)$ with $ceil(\cdot)$ being the ceiling function, $p = rem(n/N)$ if $rem(n/N) \neq 0$, and $p = N$ if $rem(n/N) = 0$ with $rem(\cdot)$ being the remainder function. The indices m_1 and n_1 are the same as those used in (16). The tensor $\tilde{\mathcal{R}}$ is then converted into another tensor with the elements $\mathcal{R}_{WB}(m', n', l) = \tilde{\mathcal{R}}(m, n, l)$. For example, if $M = 2$ and $N = 2$, then $\mathbf{R}_{WB}$ is divided into sub-matrices:

$$\mathbf{R}_{WB} = \left[\begin{array}{c|c|c|c} \mathbf{R}_{WB}^{(1,1)} & \mathbf{R}_{WB}^{(1,2)} & \mathbf{R}_{WB}^{(1,3)} & \mathbf{R}_{WB}^{(1,4)} \\ \hline \mathbf{R}_{WB}^{(2,1)} & \mathbf{R}_{WB}^{(2,2)} & \mathbf{R}_{WB}^{(2,3)} & \mathbf{R}_{WB}^{(2,4)} \\ \hline \mathbf{R}_{WB}^{(3,1)} & \mathbf{R}_{WB}^{(3,2)} & \mathbf{R}_{WB}^{(3,3)} & \mathbf{R}_{WB}^{(3,4)} \\ \hline \mathbf{R}_{WB}^{(4,1)} & \mathbf{R}_{WB}^{(4,2)} & \mathbf{R}_{WB}^{(4,3)} & \mathbf{R}_{WB}^{(4,4)} \end{array}\right], \tag{19}$$

The $\mathbf{R}_{WB}$ is then rearranged into the $4\times4\times L^2$ tensor $\mathcal{R}_{WB}$, whose vector $\mathcal{R}_{WB}(m', n', 1 : L^2)$ is given by (17) and (18) for $m' = 1, ..., 4$ and $n' = 1, ..., 4$.

After $\mathbf{R}_{WB}$ is converted into tensor $\mathcal{R}_{WB}$, the minimization problem in (15) is converted to

$$\phi_{WB} = \left\| \mathcal{R}_{WB} - \sum_{i=1}^{M_k} vec(\hat{\mathbf{\Psi}}_{tx,i}) \circ vec(\hat{\mathbf{\Psi}}_{rx,i}) \circ vec(\hat{\mathbf{\Psi}}_{tap,i}) \right\|_F^2, \tag{20}$$

Step 2: The problem (20) is solved by the best rank-M_k approximation of higher-order tensor decomposition. In this paper, we use the truncated HOSVD method [30] to decompose the correlation matrix.

The HOSVD of the tensor $\mathcal{R}_{WB}$ is defined as [31]

$$\mathcal{R}_{WB} = \mathbf{S} \times_1 \mathbf{U} \times_2 \mathbf{V} \times_3 \mathbf{W}, \tag{21}$$

where $\mathbf{S} \in \mathbb{C}^{N\times M\times L}$ is the singular value matrix; $\mathbf{U} \in \mathbb{C}^{N\times N}$, $\mathbf{V} \in \mathbb{C}^{M\times M}$ and $\mathbf{W} \in \mathbb{C}^{L\times L}$ are singular vector matrices. Equivalently, the Tucker decomposition [29]

of $\mathcal{R}_{WB}$ is

$$\mathcal{R}_{WB} = \sum_{n=1}^{N}\sum_{m=1}^{M}\sum_{l=1}^{L}\sigma_{mnl}(\mathbf{u}_n \circ \mathbf{v}_m \circ \mathbf{w}_l), \tag{22}$$

where σ_{nml} is the (m,n,l)-th element of $\mathbf{S}$ and $\mathbf{u}_n$, $\mathbf{v}_m$, $\mathbf{w}_l$ are the column vectors of $\mathbf{U}$, $\mathbf{V}$, $\mathbf{W}$, respectively.

Step 3: The best rank-M_k approximation of $\mathcal{R}_{WB}$ is

$$\hat{\mathcal{R}}_{WB} = \sum_{i=1}^{M_k}\sigma_i(\mathbf{u}_i \circ \mathbf{v}_i \circ \mathbf{w}_i), \tag{23}$$

where σ_i is the i-th largest singular value of $\mathbf{S}$. We thus obtain the estimation of $\mathbf{\Psi}_{tx,i}$, $\mathbf{\Psi}_{rx,i}$, and $\mathbf{\Psi}_{tap,i}$ from the Tucker decomposition:

$$vec(\hat{\mathbf{\Psi}}_{tx,i}) = \mathbf{u}_i, \tag{24a}$$

$$vec(\hat{\mathbf{\Psi}}_{rx,i}) = \mathbf{v}_i, \tag{24b}$$

$$vec(\hat{\mathbf{\Psi}}_{tap,i}) = \sigma_i\mathbf{w}_i. \tag{24c}$$

Setting $M_k = 1$ produces the rank-1 approximation of the wideband Kronecker model (7). The rank-1 approximation of the narrow-band Kronecker model was treated as the nearest Kronecker product (NKP) problem in [36, 37].

Alternative to HOSVD method, the correlation matrix can be decomposed by tensor model [27, 26]. The narrow-band channel correlation is characterized by the fourth-order covariance tensor $\mathcal{R}^{tN}$ whose (m_1, n_1, m_2, n_2)-th element is

$$\{\mathcal{R}^{tN}\}_{m_1n_1m_2n_2} = E_k\{h_{m_1,n_1}(k)h^*_{m_2,n_2}(k)\}. \tag{25}$$

We extend the tensor model to the wideband channel as the sixth-order tensor $\mathcal{R}^{tW}$ whose $(m_1, n_1, l_1, m_2,$

n_2, l_2)-th element is

$$\{\mathcal{R}^{tW}\}_{m_1 n_1 l_1 m_2 n_2 l_2} = E_k\{h_{m_1,n_1}(k,l_1)h^*_{m_2,n_2}(k,l_2)\}. \tag{26}$$

Here $m_1, m_2 = 1, ..., M$, $n_1, n_2 = 1, ..., N$, and $l_1, l_2 = 1, ..., L$. If we define the third-order channel tensor $\mathcal{H}(k)$ whose (m, n, l)-th element is

$$\{\mathcal{H}(k)\}_{mnl} = h_{m,n}(k,l), \tag{27}$$

then $\mathcal{R}^{tW}$ is given by

$$\mathcal{R}^{tW} = E_k\{\mathcal{H}(k) \circ \mathcal{H}^*(k)\}. \tag{28}$$

The narrow-band tensor model $\mathcal{R}^{tN}$ is a special case of (28) by setting $L = 1$.

The HOSVD of the sixth-order tensor model (26) is given by [31]

$$\mathcal{R}^{tW} = \mathbf{S}^{tW} \times_1 \mathbf{U}^{(1)} \times_2 \mathbf{U}^{(2)} \times_3 \mathbf{U}^{(3)} \times_4 \mathbf{U}^{(4)} \times_5 \mathbf{U}^{(5)} \times_6 \mathbf{U}^{(6)}. \tag{29}$$

The tensor $\mathcal{R}^{tW}$ is estimated with the M_t largest singular values and the corresponding singular vectors:

$$\hat{\mathcal{R}}^{tW} = \sum_{i=1}^{M_t} \sigma_i^{tW} \mathbf{u}_i^{(1)} \circ \mathbf{u}_i^{(2)} \circ \mathbf{u}_i^{(3)} \circ \mathbf{u}_i^{(4)} \circ \mathbf{u}_i^{(5)} \circ \mathbf{u}_i^{(6)}. \tag{30}$$

where M_t is a user-defined parameter that depends on the required accuracy. Switching the order of calculations in (30) produces

$$\hat{\mathcal{R}}^{tW} = \sum_{i=1}^{M_t} \sigma_i^{tW} (\mathbf{u}_i^{(1)} \circ \mathbf{u}_i^{(4)}) \circ (\mathbf{u}_i^{(2)} \circ \mathbf{u}_i^{(5)}) \circ (\mathbf{u}_i^{(3)} \circ \mathbf{u}_i^{(6)}). \tag{31}$$

When (31) is compared to (23), the correlation matrices are given by

$$\hat{\mathbf{\Psi}}_{tx,i} = \mathbf{u}_i^{(1)} \circ \mathbf{u}_i^{(4)}, \tag{32a}$$

$$\hat{\mathbf{\Psi}}_{rx,i} = \mathbf{u}_i^{(2)} \circ \mathbf{u}_i^{(5)}, \tag{32b}$$

$$\hat{\mathbf{\Psi}}_{tap,i} = \mathbf{u}_i^{(3)} \circ \mathbf{u}_i^{(6)}. \tag{32c}$$

Note that the outer product of the two vectors in (32) produces the correlation matrix directly while (23) yields vectorized correlation matrices. The correlation matrices estimated by (32) do not equal the correlation matrices estimated by (23). The proposed PKM-HOSVD constructs the third-order tensor and only third-order SVD is performed for decomposition. In contrast, the sixth-order tensor model needs the sixth-order SVD, which exhibits a high computational complexity.

The accuracy of the decomposition can be measured by both MSE and CMD between the original correlation matrix $\mathbf{R}$ and the reconstructed matrix $\hat{\mathbf{R}} = \sum_{i=1}^{M_k} \hat{\mathbf{\Psi}}_{tx,i} \otimes \hat{\mathbf{\Psi}}_{rx,i} \otimes \hat{\mathbf{\Psi}}_{tap,i}$. The normalized MSE is defined as

$$e(\mathbf{R}, \hat{\mathbf{R}}) = \left\| \mathbf{R} - \hat{\mathbf{R}} \right\|_F^2 / \left\| \mathbf{R} \right\|_F^2 . \tag{33}$$

The CMD is considered a better metric than MSE when measuring matrix similarity. It is defined as [32]

$$d(\mathbf{R}, \hat{\mathbf{R}}) = 1 - \frac{tr\{\mathbf{R}\hat{\mathbf{R}}\}}{\left\| \mathbf{R} \right\|_F \left\| \hat{\mathbf{R}} \right\|_F} \in [0, 1]. \tag{34}$$

The CMD becomes zero if the two matrices are identical up to a scalar factor. It becomes one if the two matrices are completely orthogonal from each other.

We extend (34) to calculate the CMD between the correlation tensors $\mathcal{R}$ and $\hat{\mathcal{R}}$:

$$d(\mathcal{R}, \hat{\mathcal{R}}) = 1 - \frac{< vec(\mathcal{R}), vec(\hat{\mathcal{R}}^*) >}{\|\mathcal{R}\|_F \left\|\hat{\mathcal{R}}\right\|_F} \in [0, 1]. \tag{35}$$

where $<, >$ is the inner product of two vectors. It is clear that if $vec(\mathcal{R})$ and $vec(\hat{\mathcal{R}}^*)$ are orthogonal then the CMD would be 1.

4 MEASUREMENT CAMPAIGN AND DATA PROCESSING

To validate the principle Kronecker model and compare different decomposition methods, we conducted several channel sounding experiments in both different frequency bands and different propagation environments. The measurement occupied a 20 MHz bandwidth centered at either 800 MHz, 2.2 GHz, or 5.2 GHz. The MIMO transmitter and receiver consisted of National Instruments (NI) multi-channel RF signal generators and RF signal analyzers. The measurement data saved in NI instruments were processed by MATLAB. The details of equipment setup, field measurement, and data processing are described in 4.1, 4.2, and 4.3, respectively.

4.1 EQUIPMENT SETUP

Figure 4.1(a) depicts the block diagram of the transmitter. The Rubidium Frequency Standard provided a common 10 MHz reference clock for PXIe-5652 which generated the local oscillator (LO) and sampling clock for the system. The baseband waveforms were generated by PXIe-5450, and the differential analog I and Q signals were generated by its build-in digital-to-analog converter (DAC). In PXIe-5611, the I/Q signals were modulated and up-converted to the desired radio frequency (RF). The RF signals were transmitted by whip antennas after the power amplifiers. We configured the transmit parameters using soft panels designed with LabView, such as bandwidth, sampling frequency, carrier frequency, and number of channels [38, 39].

Figure 4.1(b) depicts the block diagram of the MIMO receiver. The PXIe-5691 worked as the low noise amplifier in the receiver. The amplified RF signals were down-converted to intermediate frequency (IF) in the PXIe-5601. The IF signals were passed into the analog-to-digital converter (ADC) of the PXIe-5622 and demodulated

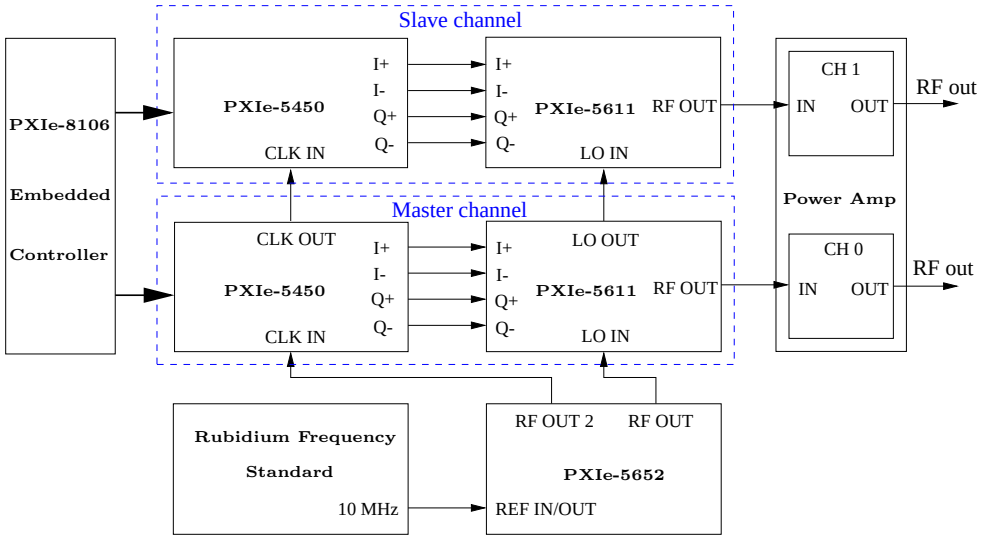

(a) Structure of the 2-channel transmitter. The power amplifiers were NI-5691 Dual RF Amplifier or RF Bay's MPA10-40. If 4-channel transmitter was desired, then two more channels were added as slave channels with two additional PXIe-5450 I/Q Signal Generators and two PXIe-5611 Modulators.

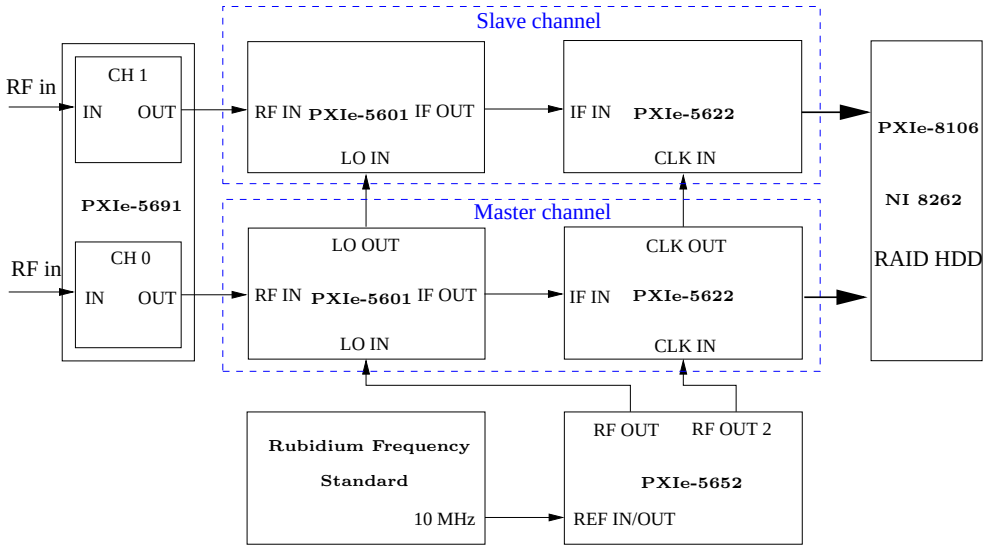

(b) Structure of the 2-channel receiver. If 4-channel receiver was used, then two additional channels were added as slave channels with two PXIe-5622 IF Digitizers and two PXIe-5601 RF Down-convertors, plus another PXIe-5691 RF Amplifier serving as the low noise amplifier.

Figure 4.1. Block diagrams of the MIMO transmitter and receiver.

into the baseband I and Q signals. For high speed acquisition, a RAID drive was used to store the acquired data for post-processing.

Four GA.107 magnetic cellular band whip antennas were used in 800 MHz and 2.2 GHz experiments, and four HyperGain Model HG2458MGRD whip antennas were used in 5.2 GHz experiment. In the indoor measurement, these antennas were placed at the four corners of one 13 $\times$ 13 cm^2 metal stool. In the outdoor measurement, they were placed on the roof of a mini-van as a 13 $\times$ 13 cm^2 square array.

4.2 MEASUREMENT ENVIRONMENTS

Measurements were conducted in the following three different environments—one indoor, two outdoor:

1) Emerson Electrical Corporation Hall (EECH) of Missouri University of Science and Technology. The floor plan of the second floor in EECH is depicted in Fig. 4.2, where the area is approximately 68 $\times$ 21 m^2. The receiver was fixed at point A1; the transmitter was fixed at the points B1, C1, D1, E1 or F1. The rooms were furnished with office desks, chairs, and cubical dividers.

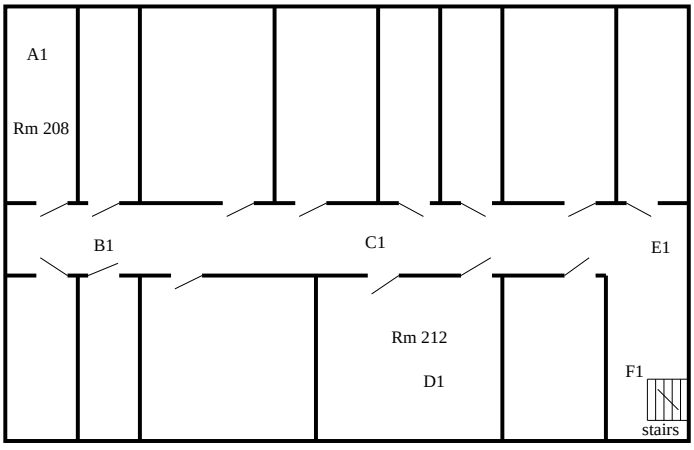

Figure 4.2. Floor plan of the second floor in Emerson Hall with labled points indicating transmitter/receiver locations.

2) US Highway 63. The roadside environment contained mostly fields with a few houses and road signs in a low to medium traffic density. Two mini-vans were roughly 50 – 150 m apart and with speeds up to 45 mph.

3) Rolla Lions Club Park. The map of the park is given in Fig. 4.3 and the park's area is approximately 0.78 km by 0.8 km. The fixed-moving cases were conducted between point P and point C. The transmitter was fixed at point P, and the receiver moved from point P, passing through point B, to arrive at point C. The receiver then returned from point C. The speed of the moving mini-van was up to 15 mph. In the moving-moving case, two mini-vans moved from point C to point G through B, A, P, D, E, and F. The moving speed was up to 20 mph.

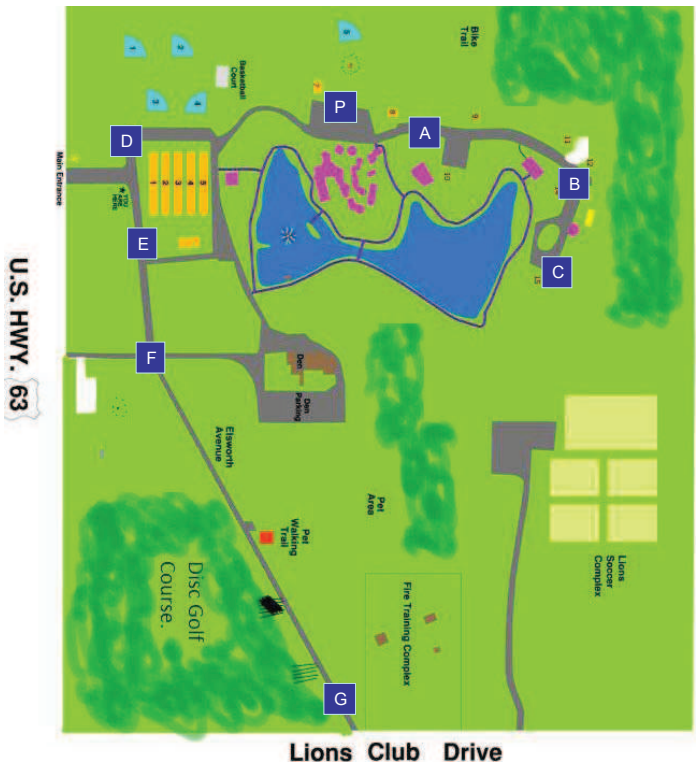

Figure 4.3. Map of Rolla Lions Club Park with labeled points indicating transmitter/receiver locations.

All of the experiments are summarized in Table 4.1. Each measurement case is defined according to the condition of the transmitter, the receiver, and the carrier frequency. For example, if the transmitter is fixed and the receiver is moving when the carrier frequency is 800 MHz, the case name is F/M-800.

Table 4.1. The description of the measurement campaign.

	Location	Case
Outdoor	US Hwy. 63	M/M-800, M/M-2200, M/M-5200
	Lions Club Park	M/M-800, M/M-2200, M/M-5200
		F/M-800, F/M-2200
Indoor	EECH	F/F-800, F/F-2200

4.3 MIMO CHANNEL PROBING SIGNALS AND CHANNEL ESTIMATION ALGORITHM

The frame structure of the probing signal at each transmit channel consisted of a BPSK block with length N_b and N_f blocks of preamble sequences with length N_p, as shown in Fig. 4.4. The BPSK block was for frame synchronization purposes and each transmitter used a 144-bit pseudo-random noise (PN) sequence. The frame synchronization was repeated after every N_f blocks of preamble transmission. The recorded I/Q signals from the hardware were typically fractionally spaced at T_s/D, where T_s is the symbol duration and D is the number of samples per symbol. We used $D = 3$ in these measurements. After synchronization, the I/Q signals were down-sampled to T_s space and saved as baseband data for channel estimation. The preamble sequence for MIMO channel sounding was the Zadroff-Chu (ZC) sequences [40, 10] of length 256, padded with cyclic prefix (CP) of length 64. The preamble structures for the 4×4 MIMO transmitters are illustrated in Fig. 4.5, where TX1˜TX4 denote four transmit channels, respectively. The 4×4 MIMO channel sounding used four preamble

blocks, where TX1 and TX2 transmitted the preamble sequences in Preamble 1 and Preamble 2, while TX3 and TX4 transmitted nothing. In Preamble 3 and Preamble 4, TX1 and TX2 transmitted nothing, while TX3 and TX4 transmitted the preamble sequences.

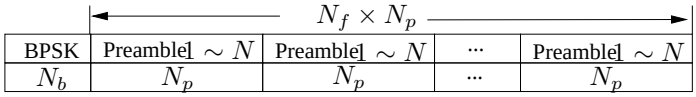

Figure 4.4. The frame structure of the transmitted signal for multi-channel sounding.

	Preamble 1		Preamble 2		Preamble 3		Preamble 4	
TX1	CP	$\mathbf{x}_{11}$	CP	$\mathbf{x}_{12}$	**0**	**0**	**0**	**0**
TX2	CP	$\mathbf{x}_{21}$	CP	$\mathbf{x}_{22}$	**0**	**0**	**0**	**0**
TX3	**0**	**0**	**0**	**0**	CP	$\mathbf{x}_{33}$	CP	$\mathbf{x}_{34}$
TX4	**0**	**0**	**0**	**0**	CP	$\mathbf{x}_{43}$	CP	$\mathbf{x}_{44}$

Figure 4.5. The signal structure of preambles for channel estimation, while **0** means no transmission.

The frequency domain Least Square (LS) method [41] was used for channel estimation, followed by time-domain truncation to channel length L. The sequences used for the 4×4 MIMO transmitter were

$$\begin{aligned}
\mathbf{x}_{11} = \mathbf{x}_{21} &= \mathrm{IFFT}_{N_{chu}}\{\mathbf{a}_{chu}\} \cdot \sqrt{N_{chu}}, \\
\mathbf{x}_{12} &= \mathrm{IFFT}_{N_{chu}}\{-\mathbf{a}^*_{chu}\} \cdot \sqrt{N_{chu}}, \\
\mathbf{x}_{22} &= \mathrm{IFFT}_{N_{chu}}\{\mathbf{a}^*_{chu}\} \cdot \sqrt{N_{chu}}, \\
\mathbf{x}_{33} &= \mathbf{x}_{43} = \mathbf{x}_{11}, \\
\mathbf{x}_{34} &= \mathbf{x}_{12}, \\
\mathbf{x}_{44} &= \mathbf{x}_{22}.
\end{aligned} \tag{36}$$

The k-th element of the Chu sequence $\mathbf{a}_{chu}$ was

$$\mathbf{a}_{chu}(k_f) = \exp\left(j\pi \frac{M_{prime}}{N_{chu}}(k_f - 1)^2\right), \quad k_f = 1, 2, ..., N_{chu}. \tag{37}$$

In our design, we chose $N_{chu} = 256$ and $M_{prime} = 1$. The CP sequences were the last 64 samples of $\mathbf{x}_{mn}$.

Let $\mathbf{y}_{mn}$ be the n-th received preamble from receiver m. Converting both the received and transmitted preambles into frequency domain yielded $\mathbf{Y}_{mn}$ and $\mathbf{X}_{mn}$, where $m = 1, ..., 4$ and $n = 1, ..., 4$. The k_f-th element in $\mathbf{Y}_{mn}$ and $\mathbf{X}_{mn}$ corresponded to the k_f-th frequency tone, and arranged $Y_{mn}(k_f)$ for all (m, n) into a matrix yielded a 4×4 matrix $\mathbf{Y}(k_f)$ for the k_f-th tone.

Let the channel matrix for the k_f-th tone be $\mathbf{H}(k_f)$ for $k_f = 1, 2, ..., N_{chu}$. Then it was estimated by

$$\hat{\mathbf{H}}(k_f) = \mathbf{Y}(k_f)\mathbf{X}^{-1}(k_f), \tag{38}$$

where $\mathbf{Y}(k_f) = \{\mathbf{Y}_{mn}(k_f)\}$, $\mathbf{X}(k_f) = \{\mathbf{X}_{mn}(k_f)\}$. Thanks to the preamble structure and the property of Chu sequences, the matrix inversion can be computed directly by

$$\mathbf{X}^{-1}(k_f) = \begin{bmatrix} \mathbf{a}^*_{chu}(k_f) & \mathbf{a}^*_{chu}(k_f) & & \\ -\mathbf{a}_{chu}(k_f) & \mathbf{a}_{chu}(k_f) & \mathbf{0} & \\ & & & \\ \mathbf{0} & & \mathbf{a}^*_{chu}(k_f) & \mathbf{a}^*_{chu}(k_f) \\ & & -\mathbf{a}_{chu}(k_f) & \mathbf{a}_{chu}(k_f) \end{bmatrix} \tag{39}$$

Then the channel impulse response was obtained by inverse FFT of the (m, n)-th elements of $\mathbf{H}(k_f)$ for $k_f = 1 : N_{chu}$ as

$$\hat{\mathbf{h}}_{m,n} = \text{IFFT}_{N_{chu}}\{\hat{\mathbf{H}}_{m,n}\}, \ m = 1, ..., 4; \quad n = 1, ..., 4. \tag{40}$$

The length of the channel $\mathbf{h}_{m,n}$ was N_{chu} after the IFFT, which was then truncated to a desired channel length L that was much smaller than N_{chu}. In the measurement, we chose $L = 50$ to cover the longest multipath channels encountered in the experiments.

Assume the length of the observing window used to calculate $\mathbf{R}$ in (3) was T_R samples. The correlation matrix was obtained by averaging over the T_R samples

$$\mathbf{R} = \frac{1}{T_R} \sum_{k=1}^{T_R} \mathbf{h}_{vec}(N_p k) \cdot \mathbf{h}_{vec}^{\dagger}(N_p k). \tag{41}$$

The channel estimation was performed every $N_p T_s$ time interval.

To estimate the spatial correlation matrices, the HOSVD of $\mathcal{R}_{WB}$ in (21) is calculated by the MATLAB tensor toolbox [42, 43].

5 EXPERIMENTAL RESULTS

In this section, we evaluate the accuracy of our HOSVD decomposition method (PKM-HOSVD). We also compare it to the Kermoal decomposition method (KM) and the higher-order tensor model (TM). Finally, we analyze the capacity with the improved channel simulation model for the triply selective Rayleigh fading channel in (13).

5.1 THE ACCURACY OF THE PKM-HOSVD

For the outdoor measurements, we divided the data into many blocks with $T_R = 100$ in each case and decomposed the correlation matrices in each block. The total number of blocks for US Highway 63 was 10,016, and for Rolla Lions Club Park this number was 15,273. We used rank-1 approximation for each block. The mean of both CMD and MSE are summarized in Table 5.1 and Table 5.2, respectively. The CMD and MSE of the PKM-HOSVD were slightly smaller than that of the KM in all cases. The PKM-HOSVD and TM achieved similar approximation accuracies.

Fig. 5.1 shows the percentage of blocks with CMD > 0.1. The reason why we chose 0.1 as the threshold is shown in Section 5.2. The percentage of blocks with CMD > 0.1 shows that more than half of the outdoor cases required higher-rank decomposition to achieve satisfactory decomposition accuracy. The percentage decreased as the rank increased for both PKM-HOSVD and TM, while TM exhibited slightly better accuracy than PKM-HOSVD of the same rank.

If we focused only on blocks whose CMD of rank-1 approximations were larger than 0.1, then we used the higher-rank approximation for the blocks. The mean of CMD and MSE are listed in Table 5.3 and 5.4, respectively. The results of the TM are omitted since the performance of the TM is similar to that of the PKM-HOSVD but

Table 5.1. Outdoor results: the CMD of rank-1 approximation with different decomposition methods.

Location	Case	Mean of CMD			No.
		PKM-HOSVD	KM	TM	
US Hwy. 63	M/M-800	0.13	0.14	0.13	1
	M/M-2200	0.043	0.045	0.043	2
	M/M-5200	0.033	0.048	0.034	3
Rolla Lions Park	M/M-800	0.17	0.19	0.18	4
	M/M-2200	0.15	0.16	0.15	5
	M/M-5200	0.050	0.057	0.050	6
	F/M-800	0.20	0.22	0.20	7
	F/M-2200	0.071	0.075	0.072	8

Table 5.2. Outdoor results: the averaged MSE of rank-1 approximation with different decomposition methods.

Location	Case	Mean			No.
		PKM-HOSVD	KM	TM	
US Hwy. 63	M/M-800	0.23	0.28	0.23	1
	M/M-2200	0.082	0.091	0.083	2
	M/M-5200	0.064	0.096	0.066	3
Rolla Lions Park	M/M-800	0.30	0.38	0.30	4
	M/M-2200	0.26	0.33	0.27	5
	M/M-5200	0.098	0.11	0.098	6
	F/M-800	0.34	0.44	0.34	7
	F/M-2200	0.13	0.15	0.14	8

with higher computational complexity. It is clear that the higher-rank approximation improved the approximation accuracy and the MSE indicates the similar trend as the CMD. We omit the MSE results for the remaining experimental results.

The averaged CMD of rank-1 approximations with different decomposition methods in the indoor experiments are summarized in Table 5.5. The 2.2 GHz transmission cannot be received at points D1 and F1 due to low transmit power and a

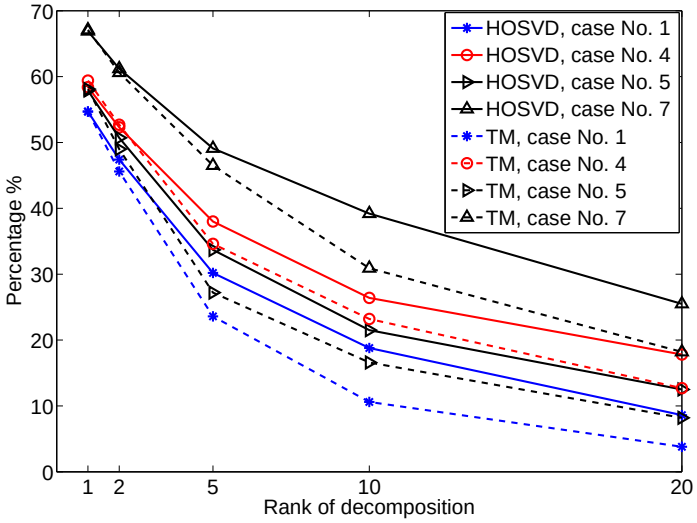

Figure 5.1. Outdoor results: percentage of blocks with CMD > 0.1.

Table 5.3. Outdoor results: the mean of CMD with higher-rank approximation for the blocks whose CMD of rank-1 approximation were larger than 0.1.

Case No.	Rank of PKM-HOSVD				
	1	2	5	10	20
1	0.19	0.16	0.12	0.094	0.070
2	0.15	0.12	0.087	0.066	0.047
3	0.18	0.12	0.089	0.069	0.053
4	0.25	0.21	0.15	0.12	0.089
5	0.20	0.18	0.13	0.10	0.075
6	0.10	0.076	0.051	0.034	0.021
7	0.27	0.23	0.17	0.13	0.098
8	0.15	0.14	0.10	0.086	0.066

Table 5.4. Outdoor results: the mean of MSE with higher-rank approximation for the blocks whose CMD of rank-1 approximation were larger than 0.1.

Case No.	Rank of PKM-HOSVD				
	1	2	5	10	20
1	0.34	0.30	0.22	0.18	0.13
2	0.27	0.23	0.17	0.13	0.092
3	0.33	0.23	0.17	0.13	0.10
4	0.42	0.37	0.27	0.22	0.17
5	0.36	0.32	0.24	0.19	0.14
6	0.20	0.15	0.10	0.068	0.042
7	0.45	0.40	0.30	0.24	0.18
8	0.28	0.25	0.20	0.16	0.13

non-line-of-sight (NLOS) environment. In the indoor experiments, rank-1 approximations were inaccurate for all of the two decomposition methods. Similar to the outdoor experiment, the PKM-HOSVD achieved better accuracy in the rank-1 approximation than the KM. The averaged CMD of the higher-rank decomposition for the indoor cases are listed in Table 5.6. It is clear that higher rank models are required for accurate decompositions to be obtained in all of the indoor cases due to the strong multi-path reflections of the wall, floor, and ceiling.

Table 5.5. Indoor results: the averaged CMD of rank-1 approximation with different decomposition methods. Rx was fixed at point A1.

Case	Location	PKM-HOSVD	KM	No.
F/F-800	B1	0.41	0.45	9
	C1	0.31	0.35	10
	D1	0.62	0.65	11
	E1	0.35	0.40	12
	F1	0.70	0.72	13
F/F-2200	B1	0.16	0.17	14
	C1	0.56	0.63	15
	E1	0.34	0.38	16

Table 5.6. Indoor results: the averaged CMD of higher-rank approximation.

Case No.	Rank of PKM-HOSVD				
	1	5	10	20	50
9	0.41	0.26	0.21	0.15	0.08
10	0.31	0.13	0.10	0.059	0.031
11	0.62	0.43	0.36	0.30	0.20
12	0.35	0.25	0.19	0.14	0.079
13	0.70	0.48	0.38	0.28	0.18
14	0.16	0.087	0.060	0.041	0.024
15	0.56	0.43	0.36	0.29	0.20
16	0.34	0.23	0.19	0.14	0.093

The 4×4 channel is not simple combination of two 2×2 channels. Due to the equipment limitations, we cannot make the larger MIMO measurement but we anticipate the 4×4 channel measurements cannot be extended to 8×8 channel easily. However, we observe that when the number of the antennas decreases, the decomposition accuracy with the same rank will increase. This means that the system with less antennas will need less ranks to achieve satisfactory decomposition accuracy in the same environment. For example, the CMD of rank-50 approximation in case No. 13 for 4×4 MIMO is 0.18. If the channel is 2×2 MIMO, then the CMD of rank-20 approximation achieves 0.11. This is intuitive in the cost function in (20) where the number of the antennas decreases, then the size of $\mathbf{\Psi}_{tx}$ and $\mathbf{\Psi}_{rx}$ would also decrease. Therefore the number of parameters which need to be estimated would decrease. Due to the page limitation, we do not include the results of 2×2 channels in the paper.

5.2 CAPACITY ANALYSIS

The MIMO channel capacity was evaluated with our improved channel simulation model (13) for triply selective Rayleigh fading channels. The original channel simulation model (10) was also included for comparison purpose.

When the channel is known to the receiver but unknown to the transmitter and assuming the power is uniformly distributed over all the transmit antennas, the capacity of a spatially correlated MIMO wide-sense stationary uncorrelated scattering (WSSUS) Rayleigh channel is given by [8]

$$C = E_k \left\{ \frac{1}{W} \int_{-W}^{W} \log_2 \det \left[\mathbf{I}_M + \frac{\beta}{N} \cdot \mathbf{H}(k,f) \cdot \mathbf{H}^{\dagger}(k,f) \right] df \right\}, \tag{42}$$

where W is the one-sided bandwidth of the baseband signal, β is the average signal-to-noise (SNR) at each receiver, and $\mathbf{H}(k,f)$ is the time-varying frequency-dependent

transfer function matrix given by

$$\mathbf{H}(k,f) = \sum_{l=0}^{L-1} \mathbf{h}(k,l) e^{-j2\pi f T_s}. \tag{43}$$

We use the improved Rayleigh fading models in [44, 45] to generate the uncorrelated Rayleigh flat fades.

Both measured and the synthesized channel capacities with not only the original but also the improved channel simulation model are shown in Fig. 5.2. In Fig. 5.2(a), the channel simulation model with a rank-1 approximation predicted the capacity reasonably well when the channel was separable and the rank-1 approximation obtained a small CMD. In contrast, Figure 5.2(b) illustrates the capacity prediction of a case whose CMD of rank-1 approximation was 0.67. In this case, the rank-1 model underestimated the capacity by 45%; the rank-100 approximation approached the true capacity to within 10%. Changes from rank-1 to rank-2 produces the largest gain in capacity estimation.

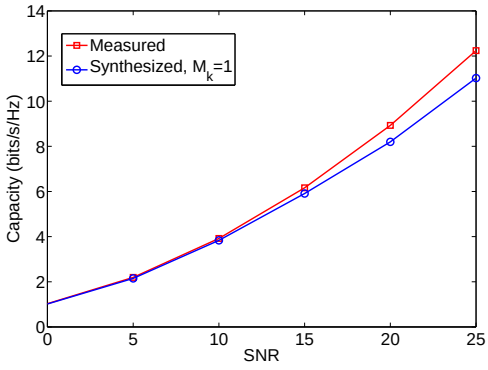

(a) The capacity of the original channel simulation model in M/M-800 case. The CMD of rank-1 approximation is 0.075.

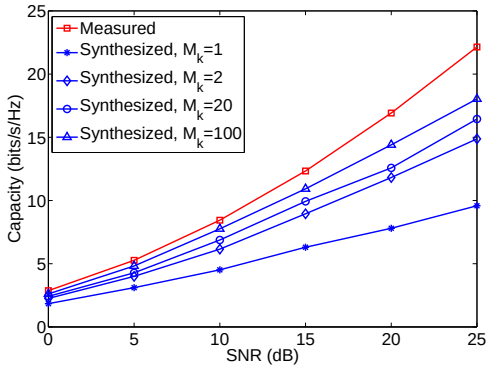

(b) The capacities of the original and improved channel simulation model in F/M-800 case. The CMD of rank-1 approximation is 0.67.

Figure 5.2. Capacities of different channel simulation models in different cases.

It is interesting to note that [24] and [46] also reported a 10%˜20% underestimate of capacity prediction from the rank-1 Kermoal method. The reason given to such a capacity error was a hypothesis that strong spatial correlation leads to a large capacity prediction error. However, our results verified that the accuracy of the capacity prediction from the Kronecker model has little to do with the correlation.

In contrast, we found that the CMD of the correlation matrix decomposition is strongly tied to the channel capacity prediction. We used the channels estimated from the M/M-800 and F/M-800 cases to draw the relationship between the CMD of the rank-1 approximation and the normalized capacity error in Fig. 5.3(a), since the mean and variance of these cases were large. We used the Curve Fitting toolbox in MATLAB to obtain the least squre fit shown as a solid line. The normalized capacity error was less than 0.21 when the CMD was less then 0.1; the normalized capacity error was less than 0.29 when the CMD was less then 0.2. We also used the modified simulation model with a rank-10 approximation for the cases whose CMD of rank-1 approximation were larger than 0.1. The relationship between the CMD of the rank-10 approximation and the normalized capacity error is shown in Fig. 5.3(b). For 94% of the cases, the capacity errors were less then 0.2.

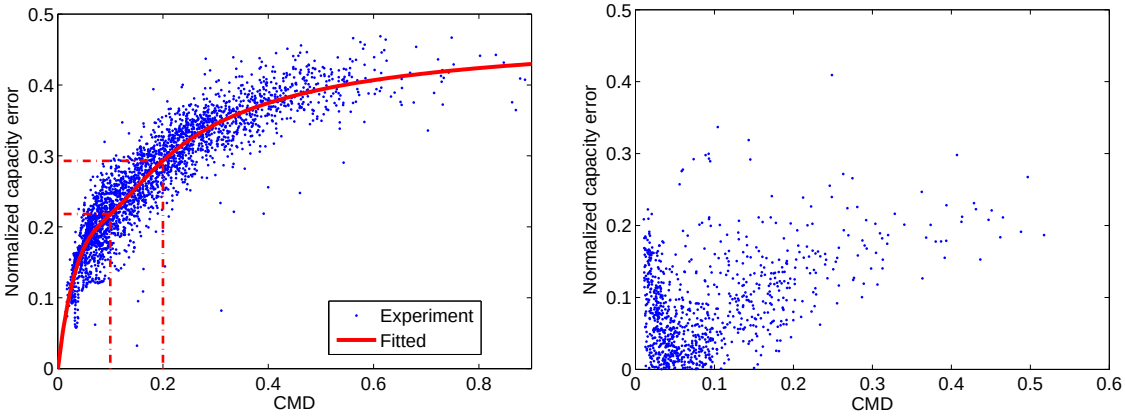

(a) The channel simulation model with rank-1 approximation.

(b) The channel simulation model with rank-10 approximation for the cases whose CMD were larger than 0.1.

Figure 5.3. Normalized capacity errors versus CMD. SNR=20 dB.

6 CONCLUSION

This paper proposes a higher-rank principle Kronecker model (PKM) for simulating triply-selective fading channels. To construct the PKM, the channel correlation matrices are decomposed using the higher-order singular value decomposition (HOSVD) method. The proposed PKM-HOSVD model improves upon the original Kronecker model by using higher-rank approximation of the channel correlation matrices rather than the rank-1 approximation. The proposed PKM-HOSVD is validated by an experimental channel-sounding campaign based on 4×4 MIMO wideband fading channels measured in both indoor and outdoor environments with carrier frequencies of 800 MHz, 2.2 GHz, and 5.2 GHz. We adopt both the CMD and MSE to evaluate the accuracy of the decomposition. Our results confirm that many practical channels must use higher-rank approximation rather than the commonly-used rank-1 approximation (or the Kermoal method) to achieve satisfactory decomposition accuracy. In addition, the proposed simulation model can predict the channel capacity more accurately than does the original rank-1 Kronecker model. We also verify that the accuracy of the capacity prediction from the Kronecker model is tied strongly to the CMD of the decomposed correlation matrices. When the CMD was less than 0.1, the normalized capacity error of rank-1 approximation was less than 0.21.

In this paper, we extract the statistic property of the channel from the channel correlation matrix. Future work includes using the slowly varying correlation matrix to design the transmitter precoder and improve the performance of the communication system.

7 REFERENCES

[1] J. Kermoal, L. Schumacher, K. Pedersen, P. Mogensen, and F. Frederiksen, "A stochastic MIMO radio channel model with experimental validation," *IEEE J. Sel. Areas Commun.*, vol. 20, no. 6, pp. 1211–1226, Aug. 2002.

[2] D. S. Shiu, G. Foschini, M. Gans, and J. Kahn, "Fading correlation and its effect on the capacity of multielement antenna systems," *IEEE Trans. Commun.*, vol. 48, no. 3, pp. 502–513, Mar. 2000.

[3] C. Xiao, J. Wu, S.-Y. Leong, Y. R. Zheng, and K. Letaief, "A discrete-time model for triply selective MIMO rayleigh fading channels," *IEEE Trans. Wireless Commun.*, vol. 3, no. 5, pp. 1678–1688, Sep. 2004.

[4] K. Yu, M. Bengtsson, B. Ottersten, D. McNamara, P. Karlsson, and M. Beach, "Modeling of wide-band MIMO radio channels based on NLoS indoor measurements," *IEEE Trans. Veh. Technol.*, vol. 53, no. 3, pp. 655–665, Mar. 2004.

[5] A. G. Zajic, G. Stuber, T. G. Pratt, and S. T. Nguyen, "Wideband MIMO mobile-to-mobile channels: geometry-based statistical modeling with experimental verification," *IEEE Trans. Veh. Technol.*, vol. 58, no. 2, pp. 517–534, Feb. 2009.

[6] M. Zhu, G. Eriksson, and F. Tufvesson, "The COST 2100 channel model: Parameterization and validation based on outdoor MIMO measurements at 300 MHz," *IEEE Trans. Wireless Commun.*, vol. 12, no. 2, pp. 888–897, Feb. 2013.

[7] F. Sharifabad, M. Jensen, and Z. Yun, "Closed-form evaluation of the MIMO channel spatial covariance," *IEEE Trans. Antennas Propag.,*, vol. 61, no. 2, pp. 901–909, Feb. 2013.

[8] A. F. Molisch, M. Steinbauer, M. Toeltsch, E. Bonek, and R. S. Thoma, "Capacity of MIMO systems based on measured wireless channels," *IEEE J. Sel. Areas Commun.*, vol. 20, no. 3, pp. 561–569, Mar. 2002.

[9] P. L. Kafle, A. Intarapanich, A. B. Sesay, J. McRory, and R. J. Davies, "Spatial correlation and capacity measurements for wideband MIMO channels in indoor office environment," *IEEE Trans. Wireless Commun.*, vol. 7, no. 5, pp. 1560–1571, May 2008.

[10] G. L. Stuber, J. R. Barry, S. W. Mclaughlin, Y. Li, M. A. Ingram, and T. G. Pratt, "Broadband MIMO-OFDM wireless communications," *Proc. IEEE*, vol. 92, no. 2, pp. 271–294, Feb. 2004.

[11] D. Sacristán-Murga, M. Payaró, and A. Pascual-Iserte, "Transceiver design framework for multiuser MIMO-OFDM broadcast systems with channel gram matrix feedback," *IEEE Trans. Wireless Commun.*, vol. 11, no. 5, pp. 1774–1787, May 2012.

[12] W. Zeng, C. Xiao, M. Wang, and J. Lu, "Linear precoding for finite-alphabet inputs over MIMO fading channels with statistical CSI," *IEEE Trans. Signal Process.*, vol. 60, no. 6, pp. 3134–3148, Jun. 2012.

[13] W. Kim, K. Lee, M.-D. Kim, J.-J. Park, H.-K. Chung, and H. Lee, "Performance analysis of spatially correlated MIMO-OFDM beamforming systems with the maximum eigenvalue model from measured MIMO channels," *IEEE Trans. Wireless Commun.*, vol. 11, no. 10, pp. 3744–3753, Oct. 2012.

[14] L. Jacobs and M. Moeneclaey, "Accurate closed-form approximation of BER for OSTBCs with estimated CSI on spatially correlated rayleigh fading MIMO channels," *IEEE Commun. lett.*, vol. 17, no. 3, pp. 533–536, Mar. 2013.

[15] P. Pan, Y. Zhang, Y. Sun, and L.-L. Yang, "On the asymptotic spectral efficiency of uplink MIMO-CDMA systems over Rayleigh fading channels with arbitrary spatial correlation," *IEEE Trans. Veh. Technol.*, vol. 62, no. 2, pp. 679–691, Feb. 2013.

[16] D. Cox, "Delay Doppler characteristics of multipath propagation at 910 MHz in a suburban mobile radio environment," *IEEE Trans. Antennas Propag.*, vol. 20, no. 5, pp. 625–635, Sep. 1972.

[17] J. Parsons, D. Demery, and A. Turkmani, "Sounding techniques for wideband mobile radio channels: a review," *IEE Proceedings I: Commun. Speech and Vision,*, vol. 138, no. 5, pp. 437–446, Oct. 1991.

[18] D. Chizhik, J. Ling, P. W. Wolniansky, R. A. Valenzuela, N. Costa, and K. Huber, "Multiple-input-multiple-output measurements and modeling in Manhattan," *IEEE J. Sel. Areas Commun.*, vol. 21, no. 3, pp. 321–331, Mar. 2003.

[19] J. Ling, D. Chizhik, D. Samardzija, and R. Valenzuela, "Peer-to-peer MIMO radio channel measurements in a rural area," *IEEE Trans. Wireless Commun.*, vol. 6, no. 9, pp. 3229–3237, Sep. 2007.

[20] R. Pirkl and G. Durgin, "Optimal sliding correlator channel sounder design," *IEEE Trans. Wireless Commun.*, vol. 7, no. 9, pp. 3488–3497, Sep. 2008.

[21] O. Renaudin, V.-M. Kolmonen, P. Vainikainen, and C. Oestges, "Non-stationary narrowband MIMO inter-vehicle channel characterization in the 5-GHz band," *IEEE Trans. Veh. Technol.*, vol. 59, no. 4, pp. 2007–2015, May 2010.

[22] F. Harrysson, J. Medbo, T. Hult, and F. Tufvesson, "Experimental investigation of the directional outdoor-to-in-car propagation channel," *IEEE Trans. Veh. Technol.*, accepted for publication.

[23] L.-C. Wang, W.-C. Liu, and Y.-H. Cheng, "Statistical analysis of a mobile-to-mobile rician fading channel model," *IEEE Trans. Veh. Technol.*, vol. 58, no. 1, pp. 32–38, Jan. 2009.

[24] H. Ozcelik, M. Herdin, W. Weichselberger, J. Wallace, and E. Bonek, "Deficiencies of 'Kronecker' MIMO radio channel model," *Electron. Lett.*, vol. 39, no. 16, pp. 1209–1210, 2003.

[25] W. Weichselberger, M. Herdin, H. Ozcelik, and E. Bonek, "A stochastic MIMO channel model with joint correlation of both link ends," *IEEE Trans. Wireless Commun.*, vol. 5, no. 1, pp. 90–100, Jan. 2006.

[26] W. Weichselberger, "On the decomposition of the MIMO channel correlation tensor," in *SITG Workshop Smart Antennas*, 2004, pp. 268–273.

[27] J. Wallace and B. Maharaj, "Accurate MIMO channel modeling: Correlation tensor vs. directional approaches," in *IEEE Global Telecomm. Conf.*, 2007, pp. 3750–3754.

[28] K. E. Baddour and N. C. Beaulieu, "Accurate simulation of multiple cross-correlated Rician fading channels," *IEEE Trans. Commun.*, vol. 52, no. 11, pp. 1980–1987, Nov. 2004.

[29] L. Tucker, "Some mathematical notes on three-mode factor analysis," *Psychometrika*, vol. 31, no. 3, pp. 279–311, 1966.

[30] L. De Lathauwer, B. De Moor, and J. Vandewalle, "On the best rank-1 and rank-(r1, r2,..., rn) approximation of higher-order tensors," *SIAM J. Matrix Analysis Applicat.*, vol. 21, no. 4, pp. 1324–1342, 2000.

[31] ——, "A multilinear singular value decomposition," *SIAM J. Matrix Anal. Applicat.*, vol. 21, no. 4, pp. 1253–1278, 2000.

[32] M. Herdin, N. Czink, H. Ozcelik, and E. Bonek, "Correlation matrix distance, a meaningful measure for evaluation of non-stationary MIMO channels," in *Veh. Tech. Conf.*, vol. 1, May 2005, pp. 136–140.

[33] Y. R. Zheng, "A non-isotropic model for mobile-to-mobile fading channel simulations," in *IEEE Military Commun. Conf.*, 2006, pp. 1–7.

[34] K. Pedersen, J. Andersen, J. Kermoal, and P. Mogensen, "A stochastic multiple-input-multiple-output radio channel model for evaluation of space-time coding algorithms," in *IEEE Veh. Tech. Conf.*, vol. 2, Sep. 2000, pp. 893–897.

[35] G. Golub and C. V. Loan, *Matrix Computations*, 2nd ed. Baltimore, MD: Johns Hopkins University Press, 1989.

[36] C. van Loan and N. Pitsianis, "Approximation with Kronecker products," in *Linear Algebra for Large Scale and Real Time Applications*. Kluwer Publications, 1993, pp. 293–314.

[37] C. van Loan, "The ubiquitous Kronecker product," *J. Computational and Applied Math.*, vol. 123, no. 1, pp. 85–100, 2000.

[38] *NI RF signal generators help*, National Instruments. [Online]. Available: `http://www.ni.com/pdf/manuals/371025k.zip`

[39] *NI RF vector signal analyzers help*, National Instruments. [Online]. Available: `http://www.ni.com/pdf/manuals/372058k.zip`

[40] D. Chu, "Polyphase codes with good periodic correlation properties," *IEEE Trans. Inf. Theory*, vol. 18, no. 4, pp. 531–532, Jul. 1972.

[41] Y. R. Zheng, M. Wang, W. Zeng, and C. Xiao., "Practical linear precoder design for finite alphabet multiple-input multiple-output orthogonal frequency division multiplexing with experiment validation," *IET Commun.*, vol. 7, no. 9, pp. 836–847, Jun. 2013.

[42] B. W. Bader, T. G. Kolda *et al.*, "MATLAB tensor toolbox version 2.5," [Online]. Available: `http://www.sandia.gov/~tgkolda/TensorToolbox/`

[43] B. W. Bader and T. G. Kolda, "Algorithm 862: MATLAB tensor classes for fast algorithm prototyping," *ACM Transactions on Mathematical Software*, vol. 32, no. 4, pp. 635–653, Dec. 2006.

[44] Y. R. Zheng and C. Xiao, "Improved models for the generation of multiple uncorrelated Rayleigh fading waveforms," *IEEE Commun. Lett.*, vol. 6, no. 6, pp. 256–258, Jun. 2002.

[45] ——, "Simulation models with correct statistical properties for Rayleigh fading channels," *IEEE Trans. Commun.*, vol. 51, no. 6, pp. 920–928, Jun. 2003.

[46] H. Ozcelik, M. Herdin, H. Hofstetter, and E. Bonek, "A comparison of measured 8×8 MIMO systems with a popular stochastic channel model at 5.2 GHz," in *Int. Conf. Telecommun.*, vol. 2, 2003, pp. 1542–1546.

SECTION

2 CONCLUSIONS

To verify the effect of linear precoder designed with instantaneous channel state information (CSI), this dissertation proposes an efficient hardware implementation scheme for iterative multi-input multi-output orthogonal frequency-division multiplexing (MIMO-OFDM) receiver. The MMSE-IC detector, channel estimator, LDPC decoder and other supporting modules are implemented in the receiver. The proposed implementation uses QR decomposition (QRD) of complex-valued matrices with four CORDIC cores and back substitution to solve the MMSE-IC problem. Compared to the existing systolic array architectures which require 15 to 38 CORDIC cores, the proposed schemes only use 4 CODIC cores but archive similar throughput. For an equivalent 4×4 MIMO with 1024 subcarrier OFDM, 16-matrix or 64-matrix pipelining can be used for proposed 4-CORDIC QRD. 1-D and 2-D array for back substitution are proposed to be combined with the two 4-CORDIC QRD schemes. The two schemes for MMSE-IC detector have been implemented on Field Programmable Gate Array (FPGA) for a baseband receiver. Their resource usage, throughput, and latency are compared with two classic systolic array architectures. The resource usage of the 16-matrix pipelining scheme is the least and the throughput is 31 clock cycles per matrix. The throughput of the 64-matrix pipelining is seven clock cycles per matrix and the resource usage is a little more than the 16-matrix pipelining scheme. The results indicate that the instantaneous CSI varies very fast in the practical system and the performance of linear precoder designed with instantaneous CSI is limited.

This dissertation also proposes a PKM for simulating triply-selective fading channels. The PKM is constructed by decomposing the channel correlation matrices with the HOSVD method. The proposed PKM-HOSVD model improves upon the

original Kronecker model by using higher-rank approximation of the channel correlation matrices rather than the rank-1 approximation. The proposed PKM-HOSVD model is validated by extensive field experiments based on 4×4 MIMO systems in both indoor and outdoor environments. The carrier frequencies in the measurement are 800 MHz, 2.2 GHz, and 5.2 GHz. Both CMD and MSE are applied to evaluate the decomposition's accuracy. These results confirm that many practical channels must use higher-rank approximation rather than the commonly-used rank-1 approximation to achieve satisfactory decomposition accuracy. This dissertation also propose that the rank-1 Kronecker model always underestimate the channel capacity but the PKM-HOSVD model can predict the channel capacity accurately by choosing different ranks. In addition, the dissertation verify that the CMD can be used to evaluate the capacity prediction's accuracy. When the CMD was less than 0.1, the normalized capacity error of rank-1 approximation was less than 0.21.

The statistic CSI extracted from the channel correlation matrix varies much more slowly than the instantaneous CSI. Future work includes using the PKM-HOSVD to design the transmitter precoder and improve the performance of the communication system.

3 PUBLICATIONS

[1] B. Han, Z. Yang, and Y. R. Zheng, "Efficient Implementation of an Iterative MIMO-OFDM Receiver Using MMSE Interference Cancelation", accepted by *IET Commun.*.

[2] B. Han, Z. Yang, and Y. R. Zheng, "FPGA Implementation of QR Decomposition for MIMO-OFDM Using Four CORDIC Cores", in *Proc. IEEE ICC*, Budapest, Hungary, Jun. 2013, pp. 4556–4560

[3] B. Han, Y. R. Zheng,"Higher-Rank Principle Kronecker Model for Triply Selective Fading Channels with Experimental Validation", accepted by *IEEE Trans. Veh. Technol.*.

[4] Z. Yang, B. Han, and Y. R. Zheng, "DSP implementation of DS/CDMA underwater acoustic modems", has been submitted to *Proc. MTS/IEEE OCEANS*, St. Johns, Newfoundland,Canada, Sep. 2014.

VITA

Bing Han received his B.S. degree in Information Electronics and Engineering from Tsinghua University, China, in 2008, and the M.S. degree in Information and Communication Engineering from the same university in 2011. He began his Ph.D. study in August 2011 at the Department of Electrical and Computer Engineering at Missouri University of Science and Technology. His research interests include channel modeling, channel estimation and equalization, and hardware implementation. He received his Ph.D. degree in Electrical Engineering from Missouri University of Science and Technology in May 2014.